Timeline of changes in spike conformational dynamics in emergent SARS-CoV-2 variants reveal progressive stabilization of trimer stalk and enhanced NTD dynamics

Authors

Sean M. Braet,[1]† Theresa S. C. Buckley,[1]† Varun Venkatakrishnan,[1]† Kim-Marie A. Dam,[2] Pamela J. Bjorkman,[2] Ganesh S. Anand[1]*

Affiliations

[1]Department of Chemistry, The Pennsylvania State University, University Park, PA.

[2]Division of Biology and Biological Engineering, California Institute of Technology, Pasadena, CA.

†Contributed equally to this work.

*Corresponding author – gsa5089@psu.edu

Abstract

SARS-CoV-2 emergent variants are characterized by increased transmissibility and each show multiple mutations predominantly localized to the spike (S) protein. Here, amide hydrogen/deuterium exchange mass spectrometry has been applied to track correlative changes in S dynamics from multiple SARS-CoV-2 variants. Our results highlight large differences across variants at two loci with impacts on S dynamics and stability. A significant enhancement in stabilization first occurred with the emergence of D614G S followed by smaller, progressive stabilization in Omicron BA.1 S traced through Alpha S and Delta S variants. Stabilization preceded progressive enhancement in dynamics in the N-terminal domain, wherein Omicron BA.1 S showed the largest magnitude increases relative to other preceding variants. Changes in stabilization and dynamics resulting from specific S mutations detail the evolutionary trajectory of

S protein in emerging variants. These carry major implications for SARS-CoV-2 viral fitness and offer new insights into variant-specific therapeutic development.

Introduction

SARS-CoV-2 was first identified in late 2019 and is the causative agent of the ongoing coronavirus pandemic (Chang et al., 2020). Extensive efforts have sparked the development of a number of vaccines and therapeutics to mitigate the effects of infection. However, the emergence of numerous variants of concern have created an additional challenge to treatment and prevention efforts. The periodic emergence of new variants of concern beginning with Alpha, and later including Delta and most recently Omicron BA.1, have contributed to surges in cases worldwide (Wassenaar et al., 2022).

SARS-CoV-2 is a member of the family *Coronavirdae* along with other human pathogens including SARS-CoV and MERS (Corman et al., 2018). The SARS-CoV-2 virion is enveloped and encapsulates a 30 kb +ssRNA genome that encodes envelope (E) protein, membrane (M) protein, spike (S) protein, as well as 16 non-structural proteins and 9 accessory proteins (Ke et al., 2020). S, a critical viral protein for SARS-CoV-2 entry that is targeted by neutralizing antibodies, plays a multifunctional role in the infection process and is therefore a target for vaccine development (Martinez-Flores et al., 2021). S is a glycosylated homotrimer with each monomer consisting of S1 and S2 subunits (Fig. 1A). The S1 domain comprises an N-terminal domain (NTD), a receptor-binding domain (RBD) and two subdomains SD1 and 2, with the RBD mediating the interaction interface with the human ACE2 receptor (Lan et al., 2020). The S2 domain includes the S1/S2 and S2 proteolytic cleavage sites as well as a fusion peptide. During the viral entry process, the S protein is processed by furin protease at the S1/S2 cleavage site either prior to or after S binding to ACE2 receptor. This enables secondary cleavage by a separate

protease (commonly transmembrane serine protease 2 (TMPRSS2) or cathepsin) at the S2 site (Peacock et al., 2021; Shang et al., 2020; Vankadari, 2020), which leads to dissociation of S1 and release of the S2 subunit to drive membrane fusion and cellular entry.

S protein plays three critical roles in facilitating host cell entry: S must bind ACE2, be proteolytically processed, and promote membrane fusion. Domain-specific investigation of S and its variants have provided insights into effects of mutations on functionalities in isolation. However, there is a need to address the composite impact of individual variants on S conformational ensembles in solution (Raghuvamsi et al., 2021). Altered conformations in mutant S proteins from variants would impact interactions of S with ACE2 and downstream functions.

Due to its key roles in viral host recognition and entry, it is unsurprising that S is a hotspot for mutations in emerging variants. A defining feature of emerging variants is each of these became more dominant over the prevailing strains, which has been attributed in part to progressively increased viral fitness (Y. Liu et al., 2022; Plante et al., 2021; Ulrich et al., 2022). Consequently, S D614G showed greater fitness than wild-type S (Plante et al., 2021), the Alpha variant S showed greater fitness than D614G S (Ulrich et al., 2022), and the Delta variant S showed greater fitness than Alpha S (Y. Liu et al., 2022), which likely contributed to surges in human infections. Among the first set of mutations that were detected in S during the early phase of the pandemic, D614G emerged as a dominant variant in 2020 (Chang et al., 2020; Pandey et al., 2021). One of the striking effects observed in a comparison of WT and D614G S proteins revealed a ~ 50X enhancement in proteolytic processing by furin (Gobeil et al., 2021).

The Alpha variant subsequently emerged in September 2020, and in addition to D614G, the S carried other mutations in NTD (del 69-70, del 144), RBD (N501Y, A570D), the furin-

binding site (P681H) and the S2 subunit (T716I, S982A, and D1118H) (Xia et al., 2021) (Fig. 1B). SARS-CoV-2 infections by the Alpha variant were replaced by a more dominant Delta variant, first identified in October 2020. The Delta variant S included mutations in the NTD (T19R, G142D, del 156-157, R158G), RBD (L452R, T478K), furin cleavage site (P681R), and the S2 subunit (D950N) (Tian et al., 2021). A more recent surge in infection has been due to the Omicron variant (BA.1) first identified in November 2021 and was the most highly mutated variant compared to wildtype (Fig. 1B) (L. Liu et al., 2022). Notably, the D614G mutation has been conserved across all major variants of concern (Wassenaar et al., 2022). Additionally, the P681R mutation found in the Delta S and Omicron BA.1 S has been found to increase pathogenicity and proteolytic processing (Y. Liu et al., 2022; Saito et al., 2021), and RBD mutations in variants of concern have been found to increase affinity for the ACE2 receptor (Han et al., 2022; Ozono et al., 2021).

98 **Fig.1**

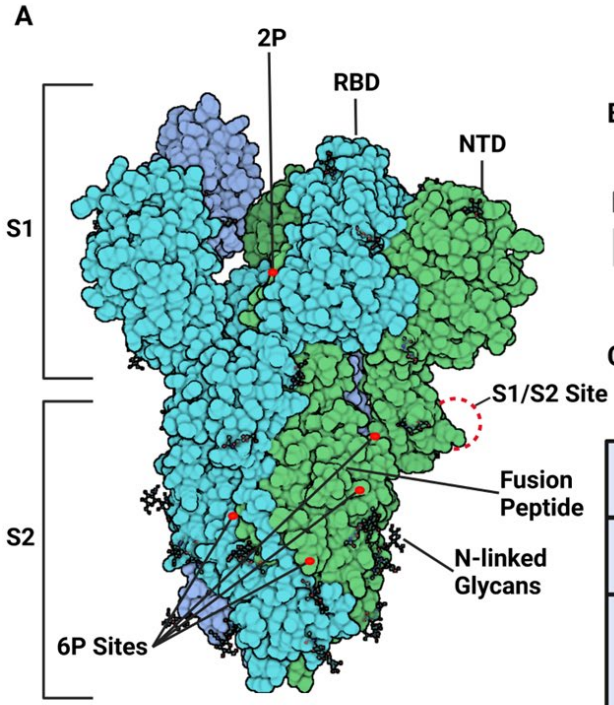

C

	NTD	RBD	S1	S2
Alpha	Δ69-70, Δ144	N501Y	A570D, **D614G**, P681H	T716L, S982A, D1118A
Delta	T19R, Δ157-158	L452R, T478K	**D614G**, P681R	D950N
Omicron (BA.1)	A67V, Δ69-70, T95I, ins214EPE, Δ211, L212I	G339D, S371L, S373P, S375F, K417N, N440K, G446S, S477N, T4978K, N501Y, Y505H	T547K, **D614G**, H655Y, N679K, P681H	N764K, D796Y, N856K, Q954H, N969K, L981F

99
100 **Fig. 1. S trimer modifications and variant mutations. (A)** S trimer (PDB:6VSB) (protomers in dark blue, teal, and
101 green) with RBD, NTD, S1/S2 site, fusion peptide, 2P substitutions (985-986), additional 6P substitutions (817, 892,
102 899, 942), and glycans. (Image created in Biorender.com) **(B)** Sequence organization for SARS-CoV-2 S protein
103 (NTD = N-terminal domain, RBD – receptor binding domain, SD1 = subdomain 1, SD2 = subdomain 2, FP = fusion
104 peptide, HR1 = heptad repeat 1, HR2 = heptad repeat 2, T.A. = transmembrane domain, I.T. = intracellular domain.
105 The brackets define the recombinant soluble S protein used in this study. Furin cleavage site (685) is indicated by
106 arrow **(C)** Mutations specific to Alpha, Delta, and Omicron BA.1 S variants. D614G is highlighted in bold.

107 A defining feature of the emergent variants is the apparent progressive increase in
108 transmissibility between humans attributable to corresponding increased viral fitness *in vitro* (Y.
109 Liu et al., 2022; Plante et al., 2021; Ulrich et al., 2022). The basis for increased viral fitness in
110 emerging variants remains poorly understood. Snapshots from single-particle cryo-EM structures
111 of SARS-CoV-2 S trimers have provided structural insights at high resolution (Cai et al., 2020;
112 Duan et al., 2020; Walls et al., 2020; Zhang et al., 2021) but do not completely capture all of the
113 interconverting conformations in solution. Multiple conformations showing RBD in 'up' or
114 'down' orientations have been observed by cryo-EM. In the trimer, these translate into closed- all

115 'down' or one, two or all 'up' conformations (Barnes, Jette, et al., 2020). These interchanging
116 conformations in solution highlight the ensemble behavior of S. Dynamics of the S ensemble are
117 fundamental to assessing trimer stability and the role of conformational substates in receptor
118 binding, proteolytic processing, and disease propagation. The ensemble properties have been
119 shown to be critical for ACE2 recognition. The RBDs of S protein have been reported to bind the
120 ACE2 receptor only in an 'up' conformation (Barnes, Jette, et al., 2020).

121 Amide hydrogen deuterium exchange mass spectrometry (HDXMS) is a useful method for
122 probing dynamic breathing motions and conformational ensembles in viral systems (Costello et
123 al., 2022; X.-X. Lim et al., 2017; X. X. Lim et al., 2017; Narang et al., 2021; Raghuvamsi et al.,
124 2021). HDXMS uses D_2O as a probe that labels backbone amides with deuterium dependent upon
125 both solvent accessibility (Peacock et al., 2018) and H-bond propensities (Englander &
126 Kallenbach, 1983). The labeling reaction can be quenched to probe time scales ranging from
127 second to days with shorter timescales impacted primarily by changes in solvent accessibility and
128 longer timescales assessing changes in H-bonding (Peacock et al., 2018). Pepsin proteolysis
129 combined with mass spectrometry provides a readout of deuterium exchange at peptide resolution
130 that can be mapped onto a structure (Hoofnagle et al., 2003). This captures dynamics (> seconds
131 timescale) of the whole ensemble. Further it offers an ability to resolve more than one slow
132 interchanging conformations (if present) by deconvolution of bimodal distributions of deuterium
133 exchanged mass spectral envelopes (Hodge et al., 2020; Hoofnagle et al., 2003; Oganesyan et al.,
134 2018). Decreased deuterium exchange reflects protection from solvent and/or enhanced stability
135 and correspondingly; increased exchange reports increased solvent accessibility and/or disorder.

136 Comparative HDXMS of recombinant wildtype, D614G, Alpha, Delta, and Omicron BA.1
137 S variants has allowed us to track changes in intrinsic dynamics across conserved regions of S

through the progressively emerging variants of concern. Our results reveal that the timeline of emergence corresponds to an overall stabilizing effect on the S trimer, together with increased dynamics in the NTD and RBD. These loci in the S2 and S1 subunits encompass sites on S showing greatest differences in deuterium exchange in non-glycosylated peptides common across all variants. Peptides showing differential deuterium exchange identified in the trimeric interface referred to as the stalk region in the rest of the study, report inter-protomer interactions while changes in the NTD and RBD report intra-protomer interactions. The D614G point mutation conferred an initial increase in stalk stabilization. This together with increased NTD dynamics in newer variants, contributed to further enhancement of both effects. Timeline analysis reveals that stabilization and enhancement of NTD dynamics effects are independent, with Delta S achieving near maximal stabilization as measured by HDXMS in our experimental timescales. Variants showed varied NTD dynamics with Omicron showing the greatest magnitude increases in NTD dynamics compared to the predecessor variants and wild-type. It is yet to be seen if NTD dynamics can continue to show increases in successive variants of concern. These underscore the coordinated importance of stalk stability together with NTD flexibility upon overall S trimer dynamics, with major consequences for ACE2 recognition, binding, and proteolytic processing.

Results

Equilibration at 37 °C (3 h incubation) shifts S ensemble toward prefusion conformation

Recombinant soluble S protein constructs have made them more accessible for structural and biophysical research by obviating the need to culture SARS-CoV-2 viruses, which require extensive safety procedures and related infrastructure. Engineered S ectodomain constructs show increased expression yields aided by ablating furin-like protease cleavage site and enhancing

stability through proline substitutions (2P) (Amanat et al., 2021) and 6P (hexapro) (Hsieh et al., 2020). These engineered constructs also eliminated the need for detergent solubilization by excluding the transmembrane C-terminal segments that are embedded in the lipid bilayer in S protein assembled on intact SARS-CoV-2 particles (Barnes, West, et al., 2020).

We carried out our HDXMS analysis with a construct containing either 2P or 6P substitutions and with the four amino acid furin cleavage motif (RRAR) substituted with a single alanine (Amanat et al., 2021). These were expressed in HEK-293T cells (Barnes, West, et al., 2020). S trimers were purified by Ni-NTA and size exclusion chromatography (SEC) as described in methods. The trimer state was independently verified by cryo-EM analysis (Barnes, Jette, et al., 2020; Barnes, West, et al., 2020). S is multiply glycosylated with 22 potential N-linked glycosylation sites (Watanabe et al., 2020). We confirmed our purified trimeric S protein was multiply glycosylated and mapped N-linked glycosylation sites by bottom-up proteomics as described in methods. Of 22 potential N-linked glycosylation sites, we identified 20 sites in wild type S, 21 glycosylation sites in D614G and Delta variant S proteins, and 19 glycosylation sites in Omicron BA.1 S (Table S1). Wild-type and variant S proteins in subsequent sections denote either a 2P (Pallesen et al., 2017) or 6P (hexapro) (Hsieh et al., 2020) as described.

We carried out comparative HDXMS on 2P and 6P engineered wild-type S protein to probe differences in dynamics. 160 non-glycosylated pepsin fragment peptides provided S sequence coverage of 53.1% (Figure 2-figure supplement 1). HDXMS was measured at time points (Dex = 1-10 min). A deuterium exchange difference map and peptide level significance testing (shown in Woods plots (Lau et al., 2021) of the two constructs) revealed no substantial differences (Δ<0.5 Da) (Figure 2-figure supplement 3-4), indicating both 2P and 6P constructs offered a common baseline for assessing differences across S variants.

The soluble S trimer constructs have been observed to show sensitivity to cold temperature treatment (Costello et al., 2022): Negative stain EM (nsEM) analysis following long-term storage at 4 ºC revealed heterogeneous S conformations indicative of trimer instability, whereas incubation at 37 ºC for 3h was found to recover a well-formed and more homogenous trimeric structure (Edwards et al., 2021). However, longer incubation times were not found to increase the proportion of S in the trimeric state. It is yet to be determined if this cold sensitivity is an inherent property of the intact S protein or is relevant only to the S trimer ectodomain constructs.

To test the effects of temperature optimization on the S trimer ectodomain, we compared HDXMS on wild-type S treated with and without a 3 h incubation at 37 ºC after flash freezing and long-term storage at –80 ºC. 170 non-glycosylated pepsin fragment peptides provided a primary sequence coverage of 53.6%, and HDXMS was measured at time points (Dex = 1-10 min) (Figure 2-figure supplement 2). A deuterium exchange heat map (% RFU) of wt S shown in Fig. 2A shows higher relative exchange on the outer edges of the trimer compared to the intratrimer core (Fig. 2A). Decreased exchange alone was observed across multiple regions of S and of high magnitude at the trimer interface (Fig. 2B and D). Decreases were most prominent for peptides in trimer stalk region of S (peptides 899-913, 988-998, 1013-1021) and other interprotomer contacts (peptides 553-568 and 32-48), indicative of increased stability following a 3h incubation at 37 ºC (Fig. 2C-E, Figure 2-figure supplement 5).

206

207 **Fig. 2.**

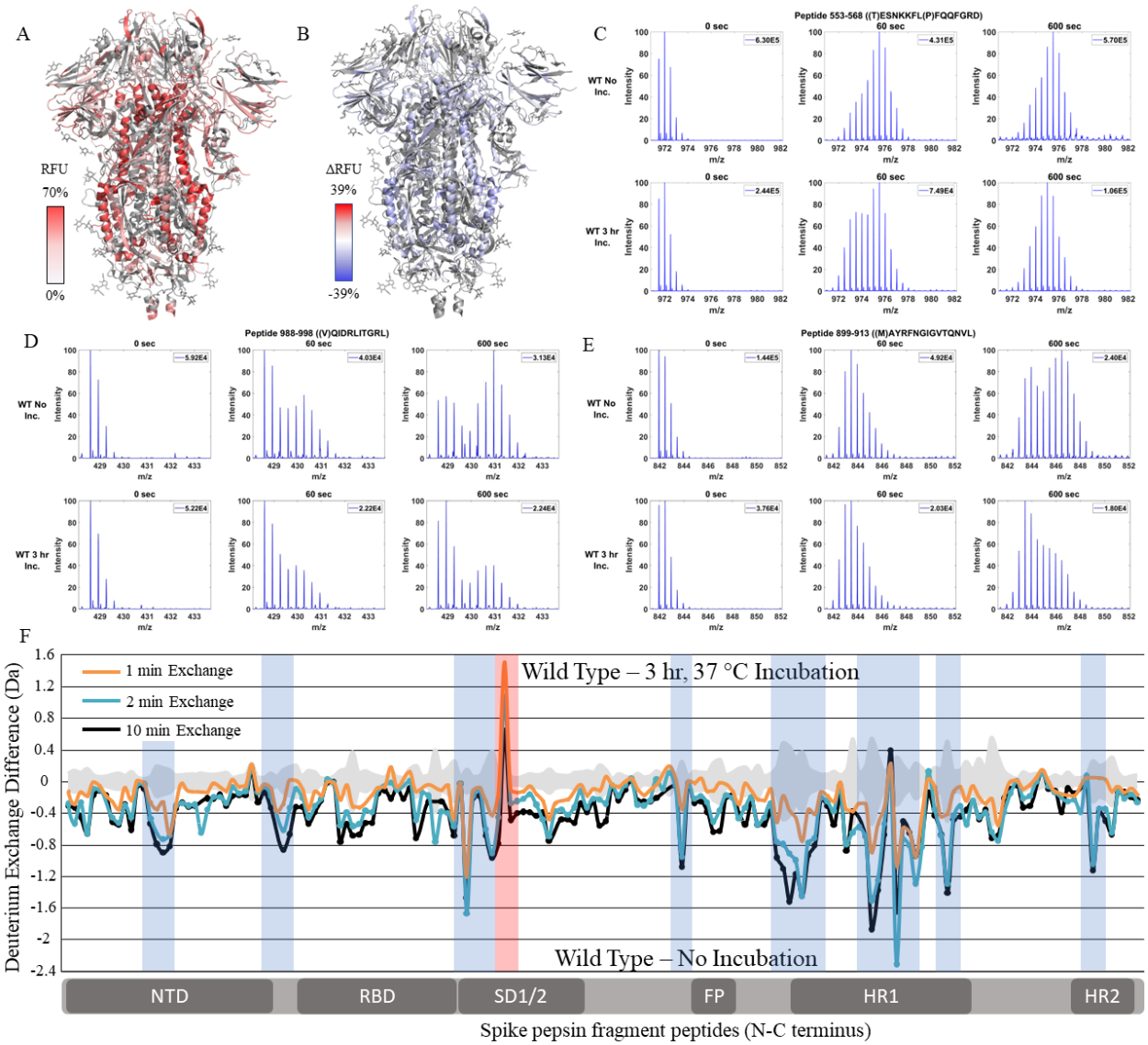

208

209 **Fig. 2. WT S trimer undergoes temperature dependent trimer-monomer transitions. (A)** Relative fractional
210 uptake (t = 10 min) for unincubated wildtype S protein mapped onto an S trimer structure with three 'down' RBDs
211 (PDB ID: 6VXX) (coverage of wildtype spike constructs shown in Figure 2-figure supplement 1-2, differences in
212 deuterium exchange for wildtype 2P and 6P constructs shown in Figure 2-figure supplement 3). White denotes low
213 deuterium exchange and shades of red denote high deuterium exchange. **(B)** Differences in deuterium exchange
214 (ΔRFU) (t = 10 min) for wildtype S protein after a 3 h incubation at 37 °C minus unincubated wild type S protein were
215 mapped onto the S protein structure (PDB ID: 6VXX). Shades of blue correspond to decreased deuterium uptake and
216 shades of red correspond to increased deuterium uptake. **(C-E)** Stacked mass spectra for wildtype S peptides 553-568,
217 899-913, and 988-998 with undeuterated reference spectra, 1 min and 10 min exchange (left to right). For each peptide,
218 the top row contains spectra for unincubated wild type S and the bottom row contains spectra for wild type S protein
219 that was incubated for 3 h at 37 °C for 3 h. **(F)** Differences in deuterium exchange (deuterons) mapped at peptide
220 resolution from N to C terminus for wild type S incubated for 3 h at 37 °C minus unincubated wildtype S are shown

in difference plots for 1, 2, and 10 min exchange. Blue boxes correspond to significantly protected peptides and red boxes correspond to significantly deprotected peptides. Significance was determined by peptide level significance testing ($p<0.01$, Figure 2-figure supplement 4-5).

Several peptides showed spectral broadening reflective of ensemble behavior in S protein in solution (Table S2). Resolvable bimodal mass spectral distributions were evident for peptides 899-913 (Table 1A) and 988-998 (Table 1B). Bimodal deuterium exchange spectra are attributable to EX1 deuterium exchange kinetics with comparable rates of protein refolding and observed rates of deuterium exchange (k_{obs}) (Kaltashov & Eyles, 2002; Weis et al., 2006). We infer that the basis for the bimodal exchange at peptides 899-913 and 988-998 that we observed in our HDXMS experimental timescales are indicative of localized trimer-protomer transitions at the interprotomer interface. Stabilization resulting from 3h 37 °C incubation is reversible. Replicate analysis of 37 °C stabilized S trimers with incubation at 4 °C prior to deuterium exchange (see methods) showed a time dependent reversal of stabilization as reported previously (Costello et al., 2022), most evident at the same peptides. These results highlight temperature sensitive reversible contacts at the edge of a trimer interface core or trimer stalk region. This region encompasses a long central helical segment (987-1031) and a helix flanking the heptad repeats (900-913) (Walls et al., 2020).

Table 1.

A

899-913	Time (min)	Left Centroid (m/z)	Right Centroid (m/z)	Left %	Right %
Unincubated WT	10	844.0	846.6	33.9	66.1
Incubated WT	10	844.3	847.2	59.3	40.7
D614G	10	843.9	845.6	90.4	9.6

B

988-998	Time (min)	Left Centroid (m/z)	Right Centroid (m/z)	Left %	Right %
Unincubated WT	10	429.1	430.9	37.4	62.6
Incubated WT	10	429.0	430.7	62.0	38.0
D614G	10	643.1	644.8	90.6	9.4

Table 1. Bimodal distributions for mass spectral envelopes of deuterium exchange in peptides 899-913 and 988-998. The left and right centroids are in mass/charge (m/z). The percentages describe the relative abundances of low (left) and high (right) exchanging populations. (A) Peptide 899-913 (B) Peptide 988-998.

Global conformational changes conferred by the D614G substitution

One of the earliest conserved mutations identified in emergent variants was D614G (Pandey et al., 2021) which demonstrated increased viral fitness along with enhanced furin proteolytic cleavage (Gobeil et al., 2021). To measure the impact of this mutation upon S dynamics, we compared HDXMS of D614G S with wild-type S. Comparative HDXMS between D614G and wild-type S protein (2P constructs) was carried out using our previously established 37 ºC temperature incubation (3h) treatment to compare equivalent trimer stabilized states. No peptides spanning the D614G mutation site were identified and therefore all peptides analyzed were common to both wild-type and D614G S. 132 non-glycosylated pepsin fragment peptides were identified covering 47.3% of the D614G sequence (Figure 3-figure supplement 1).

Relative fractional uptake values for the D614G variant mapped onto an S trimer structure (PDB 6VXX) for Dex = 10 min showed a similar relative deuterium exchange profile to that for WT S. The central stalk region showed lower exchange relative to the peripheral surface accessible regions consistent with it forming the stable core of the trimer (Fig. 3A). A difference map (D614G minus wild type) (Dex =10 min) (Fig. 3B) revealed three non-contiguous clusters of peptides distal to D614G site of mutation, showing following differences in exchange: i) Decreased exchange at trimer interface and ii) Increased exchange at NTD and iii) increased exchange in heptad repeat segments.

Fig 3.

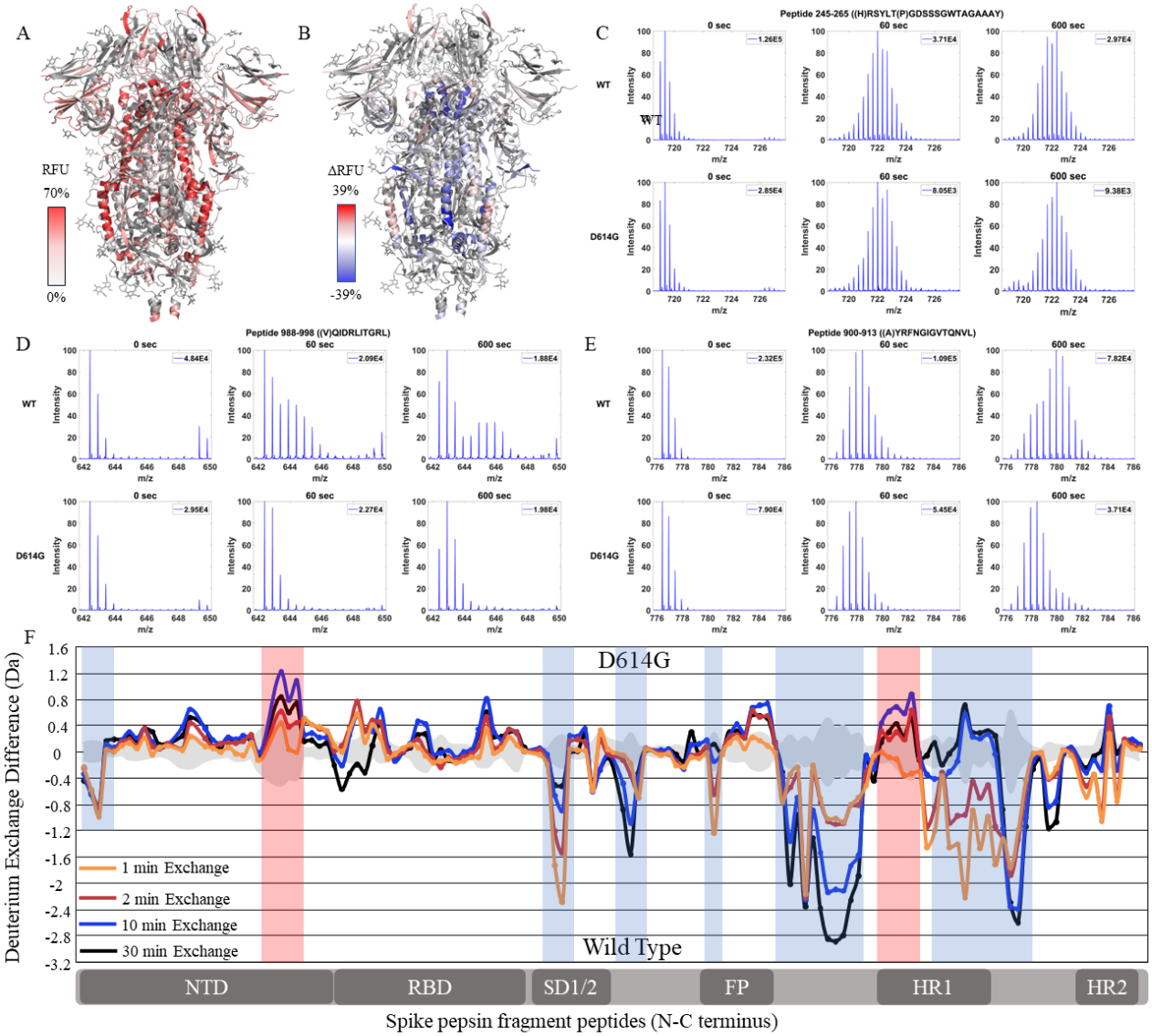

Fig. 3. The D614G mutation imparts stabilization on S trimer stalk and leads to increased NTD dynamics. **(A)** Relative fractional uptake (t = 10 min) for D614G S protein mapped onto an S protein structure (PDB ID: 6VXX) (coverage maps shown in Figure 3-figure supplement 1-2, differences in deuterium exchange for D614G S incubated at 37ºC minus D614G S without incubation is shown in Figure 3-figure supplement 3). Shades of white correspond to low deuterium exchange and shades of red correspond to high deuterium exchange. **(B)** Differences in deuterium exchange (ΔRFU) (t = 10 min) for D614G S minus wild type S protein were mapped onto an S protein structure (PDB ID: 6VXX). Shades of blue correspond to decreased deuterium uptake and shades of red correspond to increased deuterium uptake. **(C-E)** Stacked mass spectra for wildtype S peptides 245-265, 900-913, and 988-998 with undeuterated reference spectra, 1 min and 10 min exchange (left to right). For each peptide, the top row contains spectra for wildtype S and the bottom row contains spectra for D614G S. **(F)** Differences in deuterium exchange (deuterons) mapped at peptide resolution from N to C terminus for D614G minus wildtype S are shown in difference plots for 1, 2, 10, and 30 min exchange. Blue boxes correspond to significantly protected peptides and red boxes correspond to significantly deprotected peptides. Significance was determined by peptide level significance testing ($p<0.01$, Figure 3-figure supplement 4). Back exchange for D614G is estimated in Figure 3-figure supplement 5.

Decreased exchange at the trimer stalk region in D614G

Deuterium exchange difference plots showed a small subset of contiguous peptides from three regions within the trimer stalk region that showed the largest magnitude protection in deuterium exchange (Dex = 1 min) in the D614G variant (Fig. 3C, Figure 3-figure supplement 4). These regions also showed decreased exchange upon a 3 h incubation at 37 ºC (Table 2). Representative peptides 899-913, 988-998, and 1013-1021 are reporters for deuterium exchange at the stalk region (Table 2). A similar trend with decreased exchange in this locus with temperature incubation was seen with D614G S as with wild-type S (Figure 3-figure supplement 2-3). Incubating D614G S for 3 h at 37 °C resulted in a smaller degree of stabilization compared to the 3 h 37 °C incubation of WT S (Figure 3-figure supplement 3). These are consistent with stabilization observed previously for D614G (Edwards et al., 2021).

Table 2.

Peptide	Sequence	Incubated WT – Unincubated WT (ΔEx)	Incubated D614G- Unincubated WT (ΔEx)	Incubated D614G – Incubated WT (ΔEx)
899-913	MAYRFNGIGVTQNVL	-0.4 ± 0.3 Da	-1.4 ± 0.4 Da	-1.0 ± 0.4 Da
988-998	VQIDRLITGRL	-0.5 ± 0.3 Da	-1.7 ± 0.3 Da	-1.2 ± 0.3 Da
1013-1021	AEIRASANL	-0.1 ± 0.1 Da	-0.5 ± 0.1 Da	-0.4 ± 0.1 Da

Table 2. Magnitude of deuterium exchange protection conferred by D614G is greater than that by temperature stabilization. Differences in exchange (Dex =1 min) with temperature incubation for WT compared to D614G mutation for peptides from Spike trimer.

We further observed a spectral broadening of deuterium exchange in stalk peptides in wild-type S and a more resolvable bimodal distribution was observed for peptides 899-913 and 988-998 at 10 and 30 min (table S2). Peptide 899-913 lies near the base of the trimer stalk relative to RBD and exhibits a slow conformational interconversion (time scale ~ 15-30 min) in which inter-protomer contacts are broken (high exchanging population) and then reassociate (low exchanging

population). Consequently, deuterium exchange protection in mutants observed at time points later than D_{ex} = 1 min directly correlates with the rate of reversible localized trimer dissociation (Table 2). The increased strength of interprotomer contacts observed after 1 min deuterium exchange are consistent with slower transitions and a higher proportion of trimer conformations with well-formed interprotomer contacts in S variants. The protection observed after 10 and 30 min exchange is a function of increased inherent stability combined with a shift in ensemble of trimer to favor a more stable, lower exchanging conformation (Table 1). The D614G variant showed lower deuterium exchange overall indicating stronger interprotomer contacts.

Increased exchange in NTD in D614G S

A striking difference in D614G not found upon 37 ºC stabilization of wild-type S was observed in the NTD peptides (peptides spanning regions 177-191 and 243-265) (Fig. 3C, table S3), each of which showed increased exchange relative to wild-type S. This revealed that the single point mutation at D614 to glycine induced long range allosteric effects that are propagated across the trimer and are associated with both stalk stabilization and increased S1 domain dynamics at the NTD. These were the only loci outside the heptad repeats and across the S1 and S2 domains to show significant differences as shown in a Woods plot ($p<0.01$) (Figure 3-figure supplement 4) in deuterium exchange between wild-type and D614G at non-glycosylated and observed peptides. These effects provided a baseline for tracking conformational changes in S protein in emergent, more transmissible variants. The large conformational changes elicited by the D614G mutation underscore its importance as a highly conserved mutation across emergent variants (Aleem et al., 2022).

Alpha variant S shows increased exchange relative to D614G at both trimer stalk and NTD

We extended our analysis of D614G to variants of concern that each carried this mutation together with multiple other mutations (Fig. 1), comparing each subsequent variant with its epidemiological predecessor to track changes in deuterium exchange across the timeline of emergence. 45.9% coverage was obtained with 127 non-glycosylated pepsin fragment peptides common to D614G, Alpha, and wild-type S for a comparative HDXMS (Dex = 1-30 min) analysis of the Alpha variant S versus D614G S (Figure 4-figure supplement 1). Relative fractional uptake for the Alpha variant was mapped onto a wild type S structure (PDB 6VXX) (Fig. 4A). Differences in deuterium uptake (ΔRFU) for the Alpha variant S minus D614G S are mapped onto PDB 6VXX in Fig. 4B. The Alpha variant S showed lower magnitude changes in deuterium exchange relative to D614G than D614G showed compared to wildtype, particularly in the stalk region. Changes in deuterium exchange were primarily observed at the NTD for common peptides (Figure 4-figure supplement 2).

354 **Fig. 4.**

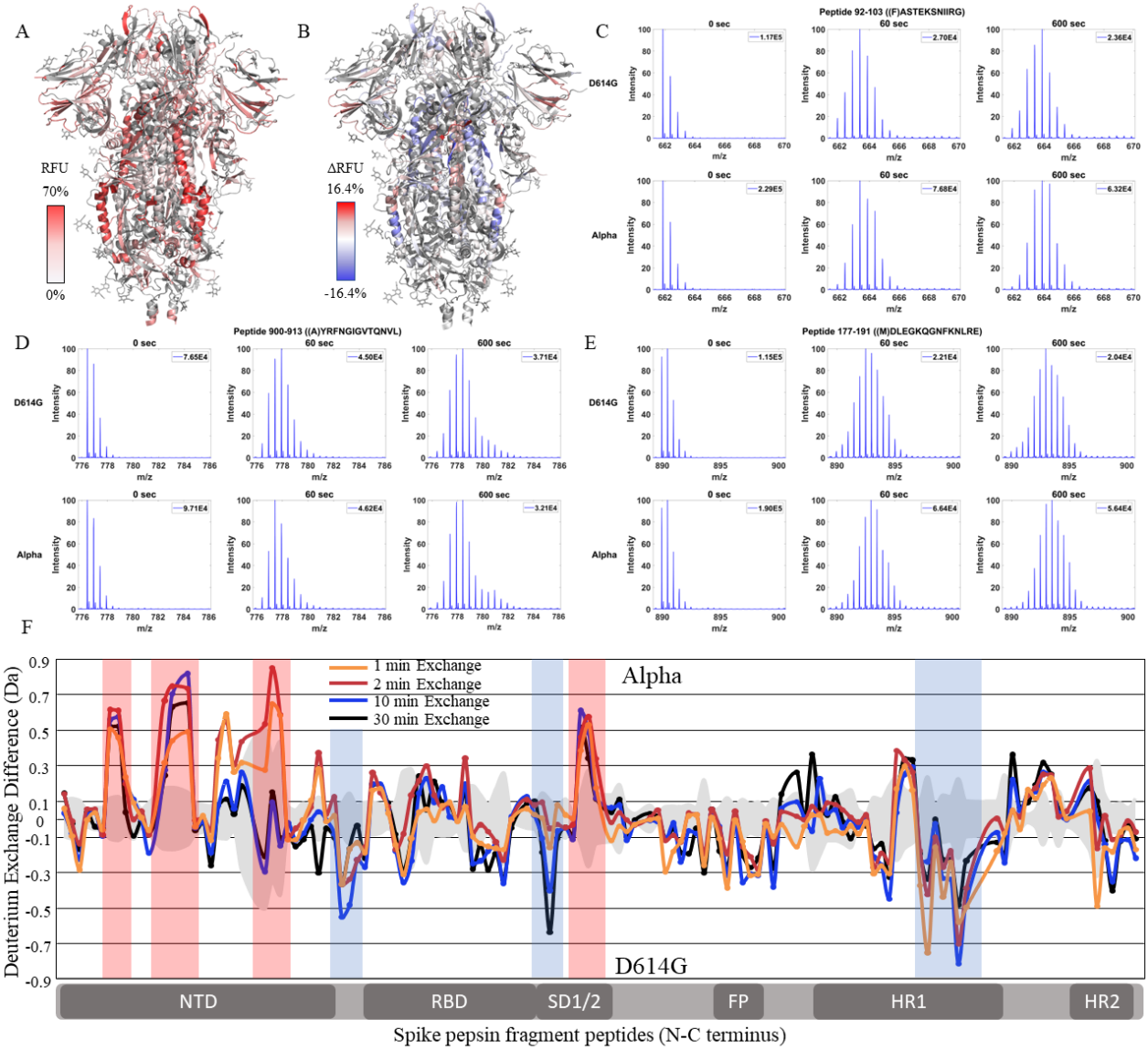

355

356 **Fig. 4. The Alpha S show significantly increased NTD dynamics. (A)** Relative fractional uptake (t = 10 min) for
357 Alpha S protein mapped onto an S protein structure with three down RBDs (PDB ID: 6VXX) coverage map is shown
358 in Figure 4-figure supplement 1). Shades of white correspond to low deuterium exchange and shades of red correspond
359 to high deuterium exchange. **(B)** Differences in deuterium exchange (ΔRFU) (t = 10 min) for Alpha S protein minus
360 D614G S protein were mapped onto an S protein structure (PDB ID: 6VXX). Shades of blue correspond to decreased
361 deuterium uptake and shades of red correspond to increased deuterium uptake. **(C-E)** Stacked mass spectra for
362 wildtype S peptides 92-103, 177-191, and 900-913 with undeuterated mass spectral envelope as reference , 1 min and
363 10 min exchange (left to right). For each peptide, the top row contains spectra for D614G S and the bottom row
364 contains spectra for Alpha S. **(F)** Differences in deuterium exchange (deuterons) mapped at peptide resolution from
365 N to C terminus for Alpha S minus D614G S are shown in difference plots for 1, 2, 10, and 30 min exchange. Blue
366 boxes correspond to significantly protected peptides and red boxes correspond to significantly deprotected peptides.
367 Significance was determined by peptide level significance testing ($p<0.01$, Figure 4-figure supplement 2).

368

In the trimer stalk region for the Alpha S, changes in deuterium exchange in Alpha relative to D614G S proteins were far lower in magnitude than in D614G relative to wildtype in the trimer stalk region. The trimer stalk region in particular showed no differences relative to wild-type S, with peptides 900-913 and 990-998 showing a small magnitude increase in deuterium exchange (0.2-0.3D) (Table 3). This indicated that a bulk of the stabilization of the stalk region in the Alpha S protein was contributed by the conserved D614G mutation.

Table 3.

Peptide	Sequence	Alpha – D614G (ΔEx)	Delta – D614G (ΔEx)	Omicron – D614G (ΔEx)
900-913	AYRFNGIGVTQNVL	-0.1 ± 0.4 Da	-0.3 ± 0.4 Da	-0.3 ± 0.4 Da
990-998	IDRLITGRL	0.1 ± 0.3 Da	-0.2 ± 0.3 Da	-0.2 ± 0.3 Da
1013-1021	AEIRASANL	0.2 ± 0.2 Da	0 ± 0.1 Da	0 ± 0.1 Da

Table 3. Deuterium Exchange protection at trimer stalk peptides in variants relative to D614G S.

Outside the stalk, a lower magnitude decrease in exchange was observed in the S2 domain specifically at peptides at the C-terminal end of heptad repeat 1 in the 940-975 region (Δ Ex= 0.4-0.8 D) as well as peptide 553-568 (Δ Ex = 0.6 D), which mediates inter-monomer contacts. Interestingly, the largest changes were observed in the NTD. The Alpha S showed increased exchange at peptides spanning 92-103, 177-191, and 201-264 (table S3).

Delta variant S shows decreased exchange at both the trimer stalk and NTD

Comparative HDXMS of the Delta variant S to the Alpha S generated 47.0% coverage was obtained with 123 non-glycosylated pepsin fragmentation peptides common to D614G and the Delta and Alpha S variants (Figure 5-figure supplement 1). RFU for Dex = 1 min in the Delta

variant and differences in exchange for Delta S minus Alpha S (Δ RFU) were mapped onto an S structure (PDB: 6VXX) (Fig. 5A, B). Delta S showed mostly decreased exchange relative to the Alpha S with decreases primarily in the trimer stalk, other S2 domain peptides, and the NTD (Fig. 5C-E). Delta S showed decreased exchange in trimer stalk peptides relative to Alpha S (Table 3). In the S2 domain, additional decreases in exchange were observed at regions 820-830 (ΔEx = 0.7D) corresponding to the fusion peptide and 900-940 (ΔEx = 1.2D) corresponding to the N-terminal end of heptad repeat 1. Based on Woods plots analyses ($p<0.01$), insignificant differences in deuterium exchange were observed for other S2 peptides relative to Alpha (Figure 5-figure supplement 2).

Delta S also showed decreased exchange for NTD peptides relative to Alpha S. Decreased exchange was most prominent at peptides spanning 92-103, 177-191, and 200-265 (Table S3). Additional decreases in exchange were observed at 306-317 (ΔEx = 0.6D) while increased exchange was observed at the RBD peptide 453-467 (ΔEx = 0.6D). Incremental decreases in exchange at the trimer stalk were in addition to a bulk stabilization imparted by the D614G mutation while decreased exchange in the NTD represented a reversal of the increased NTD exchange observed in Alpha S.

Fig. 5.

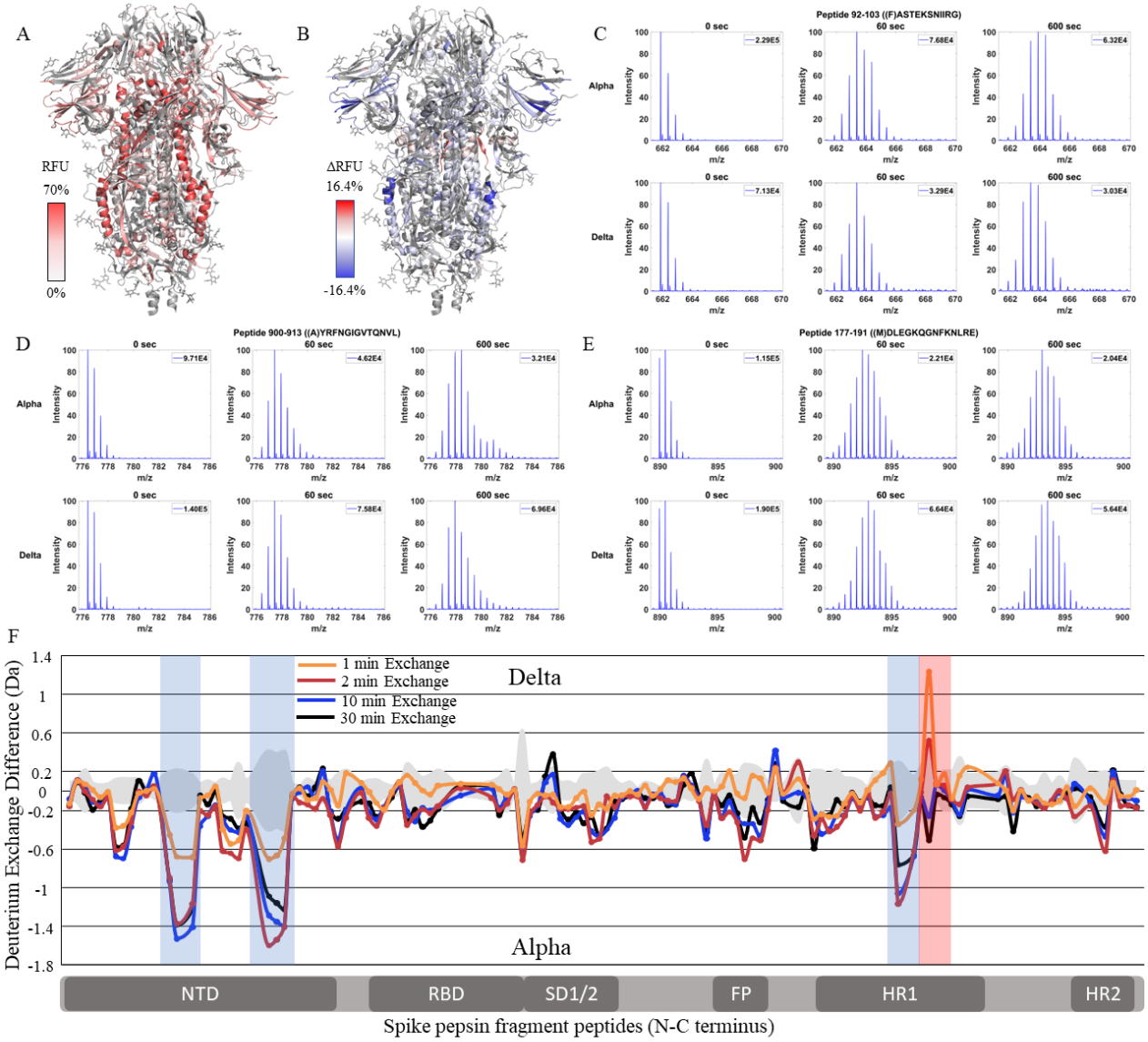

Fig. 5. The Delta variant show increased stability with decreased NTD dynamics. (A) Relative fractional uptake (t = 10 min) for Delta S protein mapped onto an S protein structure with three down RBDs (PDB ID: 6VXX) coverage maps shown in Figure 5-figure supplement 1). Shades of white correspond to low deuterium exchange and shades of red correspond to high deuterium exchange. **(B)** Differences in deuterium exchange (ΔRFU) (t = 10 min) for Delta S minus Alpha S were mapped onto an S protein structure (PDB ID: 6VXX). Shades of blue correspond to decreased deuterium uptake and shades of red correspond to increased deuterium uptake. **(C-E)** Stacked mass spectra for wildtype S peptides 92-103, 177-191, and 900-913 with undeuterated reference spectra, 1 min and 10 min exchange (left to right). For each peptide, the top row contains spectra for Alpha S and the bottom row contains spectra for Delta S. **(F)** Differences in deuterium exchange (deuterons) mapped at peptide resolution from N to C terminus for Delta S minus Alpha S are shown in difference plots for 1-, 2-, 10-, and 30-min exchange. Blue boxes correspond to significantly protected peptides and red boxes correspond to significantly deprotected peptides. Significance was determined by peptide level significance testing ($p<0.01$, Figure 5-figure supplement 2).

Omicron BA.1 S variant retains low exchange at the trimer stalk while showing increased deuterium exchange at NTD peptides

Finally, we compared Omicron BA.1 S to Delta S. 36.4% coverage was achieved with 98 non-glycosylated pepsin fragment peptides common to D614G, Delta and Omicron BA.1 S proteins (Figure 6-figure supplement 1). RFU for Dex = 1 min in Omicron BA.1 S and differences in exchange for Omicron BA.1 S minus Delta S (Δ RFU) were mapped onto an S structure (PDB: 6VXX) (Fig. 6A, B). It should be noted that the Omicron BA.1 variant used for analysis was the 6P construct, necessitated by poor expression and heterogeneity of the 2P construct of Omicron BA.1 S. Based on our analysis of wildtype S, the 2P and 6P constructs showed no differences in HDXMS. The Omicron BA.1 S showed slightly decreased exchange at the trimer stalk with increased exchange at other S2 domain peptides, and increased exchange in the NTD (Fig. 6C-E).

A small additional decrease in exchange was observed for peptides spanning the trimer stalk (Table 3). Notably, the Omicron BA.1 S showed a decrease in the higher exchanging population for stalk peptides suggesting both an impact on inherent trimer stability and ensemble behavior. In S2 domain peptides spanning 920-988 (ΔEx = 0.5-1.5D), 818-830 (ΔEx = 0.4-0.8D), and 750-756 (ΔEx = 0.6D), increased exchange was observed (Figure 6-figure supplement 2).

In the NTD, significantly increased exchange was observed in Omicron BA.1 S relative to Delta S. Increases were seen at peptides spanning 177-191, 243-265, and 306-317 (table S3). Additional increases in exchange were observed for RBD peptide 456-467 (ΔEx = 0.5D) and peptides 553-568 (ΔEx = 0.5D) and 627-643 (ΔEx = 0.5D). Omicron BA.1 S was distinct from the Alpha and Delta S proteins in that it adhered to the continued trend of decreased exchange at the trimer stalk and increased exchange in the NTD that were first observed in D614G S.

448 **Fig. 6.**

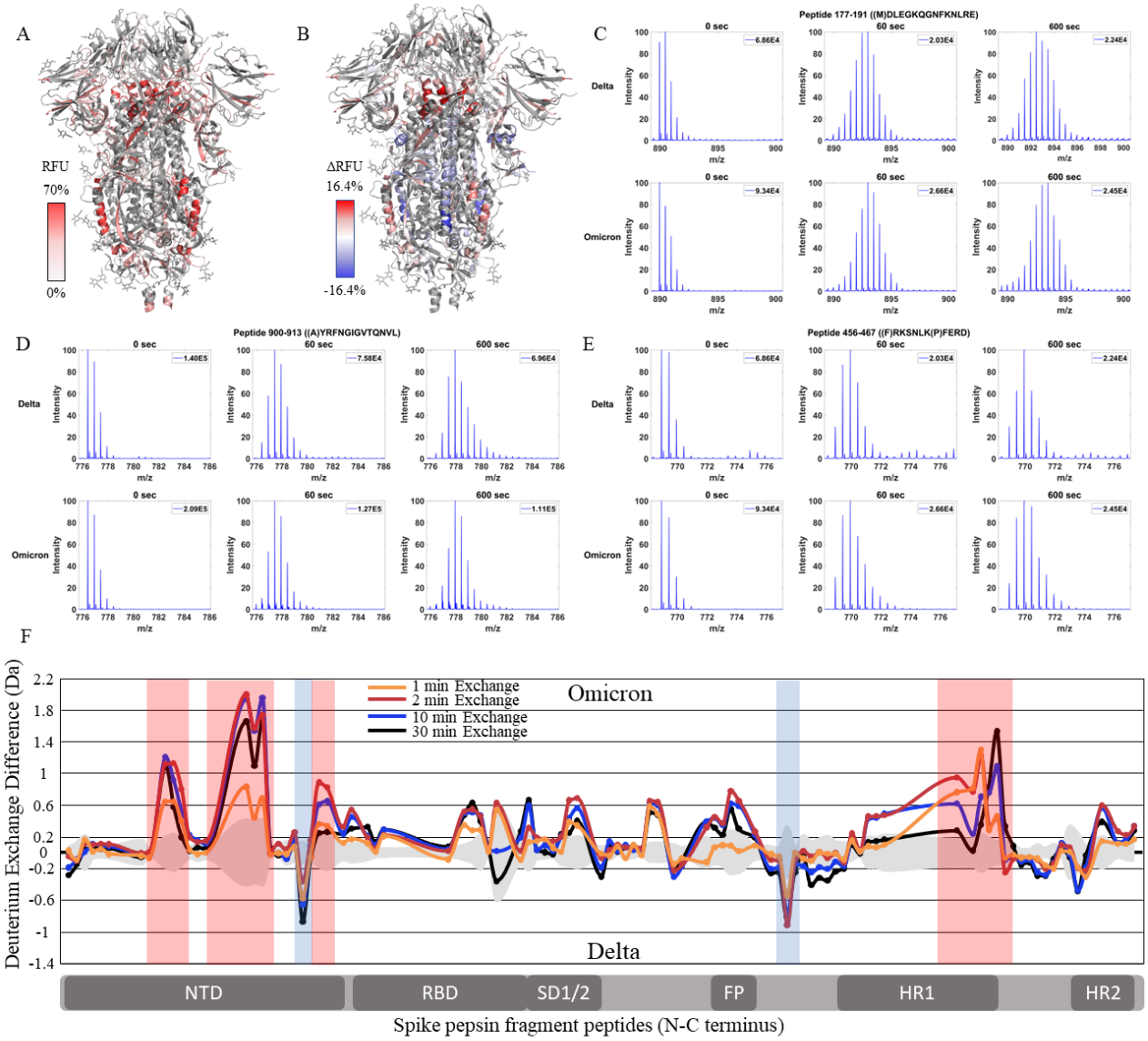

449

450 **Fig. 6. The Omicron BA.1 S shows high magnitude trimer stability and NTD dynamics. (A)** Relative fractional
451 uptake (t = 10 min) for Omicron BA.1 S mapped onto an S protein structure with three down RBDs (PDB ID: 6VXX)
452 coverage maps shown in Figure 6-figure supplement 1). Shades of white correspond to low deuterium exchange and
453 shades of red correspond to high deuterium exchange. **(B)** Differences in deuterium exchange (ΔRFU) (t = 10 min)
454 for Omicron BA.1 S minus Delta S were mapped onto an S protein structure (PDB ID: 6VXX). Shades of blue
455 correspond to decreased deuterium uptake and shades of red correspond to increased deuterium uptake. **(C-E)** Stacked
456 mass spectra for wildtype S peptides 92-103, 177-191, and 900-913 with undeuterated reference spectra, 1 min and
457 10 min exchange (left to right). For each peptide, the top row contains spectra for Delta S and the bottom row contains
458 spectra for Omicron BA.1 S. **(F)** Differences in deuterium exchange (deuterons) mapped at peptide resolution from N
459 to C terminus for Omicron BA.1 S minus Delta S are shown in difference plots for 1-, 2-, 10-, and 30-minute exchange.
460 Blue boxes correspond to significantly protected peptides and red boxes correspond to significantly deprotected
461 peptides. Significance was determined by peptide level significance testing ($p<0.01$, Figure 6-figure supplement 2).
462
463

Discussion

Changes in S conformation: Implications for viral fitness: We report two uncorrelated effects of mutations upon the conformational dynamics of variant S proteins. One of the striking observations from our comparative HDXMS analysis is the progressive stabilization of the S trimer with successive emergent S variants from D614G through Alpha and Delta and subsequently to Omicron BA.1 at the S trimer stalk region. Ensemble behavior is clearly evident from HDXMS of 3 representative peptides from wild-type S. The ensemble shifted to favor a more stable conformation upon incubation at 37 °C. Interestingly, the sequences of the 3 peptides examined in the stalk region adopt an amphipathic helical fold (Figure 7-figure supplement 1). Cold sensitivity followed by spike stabilization at higher temperatures (37°C) can be attributed to the hydrophobic interactions at the stalk region that contribute to stability at the trimer interface (Costello et al., 2022; Edwards et al., 2021; Privalov, 1990).

A first mutation to confer a large stabilization effect was D614G, a lynchpin S mutation, which appeared early during the pandemic and is conserved across nearly all recent emergent SARS-CoV-2 variants of concern (Pandey et al., 2021). Stabilization (associated with decreased exchange) at this stalk locus region showed a leveling off with Delta S (Figure 7-figure supplement 2). Comparative analysis of peptides encompassing mutations in variant S with D614G S further validated D614G being the most prominent contributor to enhanced trimer stabilization (Table S4). However, enhancement in NTD/RBD dynamics appeared more pronouncedly in Omicron BA.1 S protein. Importantly, incubation at 37 °C generated a stabilization in the stalk region but did not elicit any changes at the NTD/RBD, indicating that stalk stabilization and enhancement of NTD/RBD dynamics are uncorrelated conformational effects.

Early studies on spike trimers from HIV-1, MERS, and SARS-CoV (Derking & Sanders, 2021; Kirchdoerfer et al., 2018; Pallesen et al., 2017)highlighted analogous stem loci to comprise a conformational dynamic switch to toggle from prefusion to postfusion conformations. To overcome the conformational heterogeneity in SARS-CoV and MERS spike trimers, 2 consecutive proline substitutions were shown to confer improved expression of prefusion trimers (Kirchdoerfer et al., 2018; Pallesen et al., 2017). These mutations were extended to SARS-CoV-2 S protein. The SARS-CoV-2 2P constructs were also found to be more immunogenic, making it a preferred construct for vaccine development (Hsieh et al., 2021; Lien, Kuo, et al., 2021; Lien, Lin, et al., 2021). Mutations introduced on a 2P background were screened for improved expression and 4 additional proline substitutions were identified. These formed the basis for the hexapro (6P) (Hsieh et al., 2020) substitution construct also widely used for structural and biophysical characterization of S. Interestingly, one of the loci where we observed the biggest stabilization in D614G and successive emergent variants is at this locus. A peptide directly C-terminal to the 2P substitutions, 988-998, showed ensemble behavior across S proteins from all variants examined in this study. Omicron BA.1 S showed the highest stabilization at this locus. These independent effects of structure-guided mutations and effects from emergent variants confirm an evolutionary advantage that stabilization of the S trimer stalk region conferred SARS-CoV-2.

Increasing transmissibility (viral fitness) correlates with more stable trimer and dynamic NTD. Increased transmissibility is a defining feature of S across SARS-CoV-2 variants, with the Omicron BA.1 showing the fastest rate of infection spread (Araf et al., 2022; Y. Liu et al., 2022; Plante et al., 2021; Ulrich et al., 2022). It should be noted that increased transmissibility as assessed from the above referenced *in vitro* studies examining infection of cell lines does not linearly extrapolate to transmissibility in human populations. Comparative HDXMS revealed large

scale changes in S conformation across variants. We surmise that these conformational changes would majorly impact multiple functions of the S protein including ACE2 recognition and binding, proteolytic processing by furin-like proteases and TMPRSS2, and efficiency of membrane fusion. The conformational changes identified from changes in deuterium exchange encompassed increased compactness of a central stalk region and variable changes across NTD and RBD regions. Increased transmissibility could be attributable at least in part to a combination of the above conformational changes observed across S variants.

Comparative HDXMS of S variants relative to wild-type S at conserved amino acids revealed that the largest magnitude decreases in exchange were entirely localized to the S2 subunit (Fig. 3). One of the striking features are three key pepsin fragment peptides that are structurally non-contiguous and showed the largest decreases in exchange as well as a progressive shift in ensemble behavior that correlate with timeline of emergence. These 3 peptides spanning the stalk region represent critical trimer interface loci for maintaining a canonical prefusion conformational ensemble (Fig. 7A). Each of these 3 peptides showed differences in magnitude of protection across variants relative to wild-type S in the timescales of HDXMS (t=1- 30 min) (Fig. 7B).

HDXMS clearly demonstrates that not all mutations elicit equivalent changes in conformation/stability, some mutations have disproportionately larger impacts on overall S and trimer conformational interconversion and stability. However, non-linear improvements in trimer stability beyond that conferred by the D614G mutation likely contribute to improved efficacy in S trimer packaging on the SARS-CoV-2 virion. Due to the multiplicative effects of trimer stability on S functions, we postulate that the enhanced stability beyond that conferred by the D614G mutation could account for some of the increased viral fitness observed in Delta and Omicron BA.1 variants (Fig. 7B).

533 **Fig. 7.**

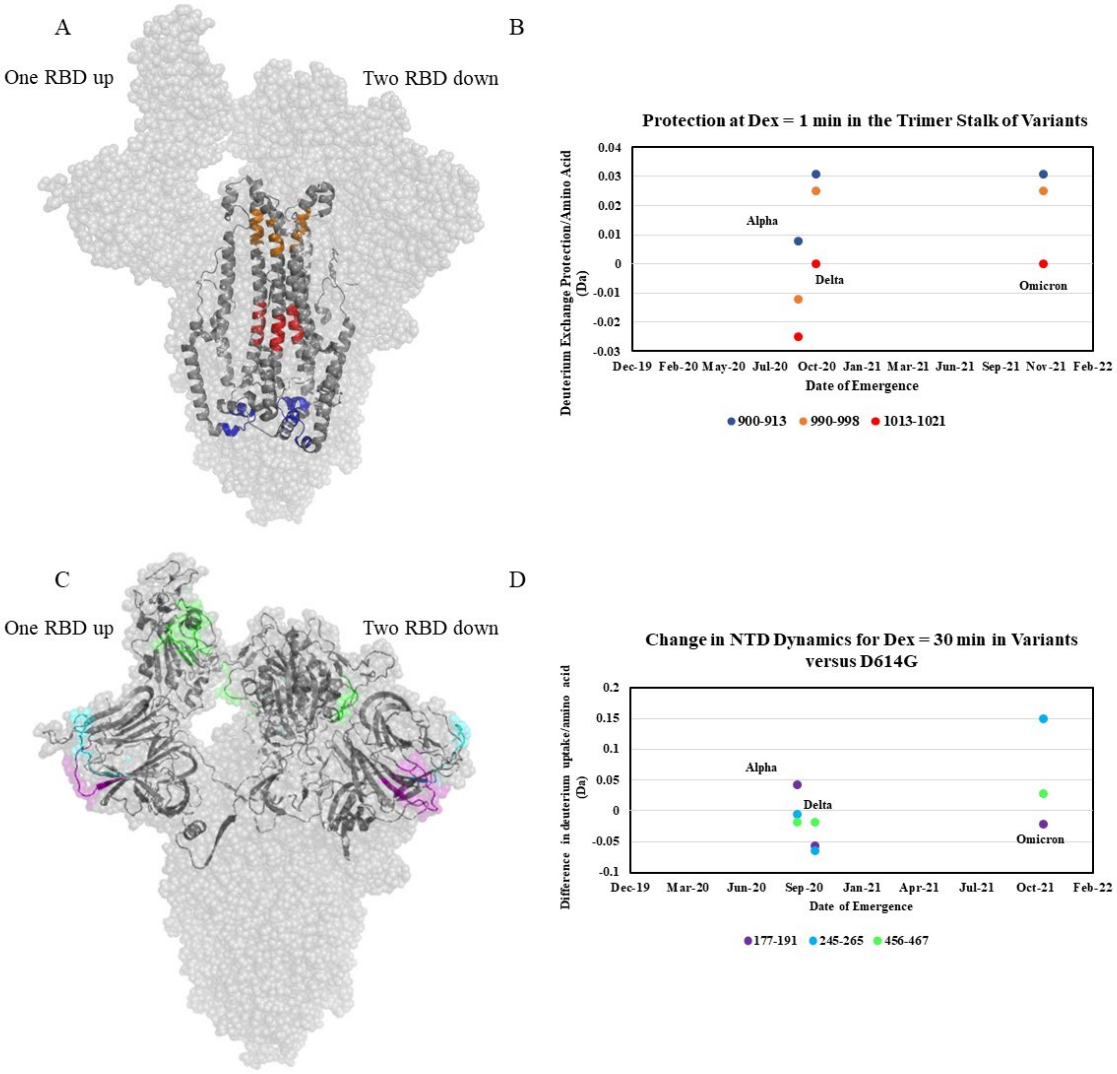

534
535 **Fig. 7. Increased trimer stability and NTD dynamics correlate with the timeline of emergence. (A)** Trimer stalk
536 peptides 900-913 (blue), 990-998 (orange) and 1013-1021 (red) mapped onto a wildtype S protein structure (PDB ID:
537 7TGX) (helical wheel analysis of stalk peptides shown in Figure 7-figure supplement 1). **(B)** Protection in trimer stalk
538 peptides in S variants compared to D614G S plotted as protection per amino acid versus date of emergence at Dex =
539 1 min. **(C)** NTD and RBD peptides showing increased dynamics in the timeline of variant emergence mapped onto a
540 1 RBD 'up' wildtype S structure (PDB ID: 7TGX). Peptides 177-191, 245-265, and 456-467 are shown in purple,
541 cyan, and green, respectively. **(D)** Changes in deuterium uptake for NTD and RBD peptides in variant S proteins
542 compared to D614G S at Dex = 30 min are plotted as change in deuterium uptake versus date of emergence (additional
543 plots in Figure 7-figure supplement 2).
544

545 Additionally, we mapped increases in dynamics at the NTD and RBD in the S1 subunit,

546 with Omicron BA.1 S showing the highest overall NTD and RBD dynamics (Fig. 7 C and D).

These changes are likely associated with the role of NTD and RBD dynamics in promoting improved ACE2 recognition and correspondingly increased viral entry across successive variants (Qing et al., 2021). Increased NTD dynamics might facilitate RBD 'up' transitions. This, coupled with mutations at the S-ACE2 interface would then facilitate increased efficacy of SARS-CoV-2 host entry. It should be noted that HDXMS reports an average deuterium exchange for an ensemble of conformations when the rates of conformational interconversion are faster relative to rates of exchange at relevant experimental conditions (Hoofnagle et al., 2003). HDXMS results mapped onto a single endstate cryo-EM structure are useful in identifying dynamic loci on the S protein. However, this leads to a distorted view of uniform changes in exchange average across conformational changes throughout the S trimer, since the endstate structure does not represent the entire conformational ensemble. HDXMS of S protein under the experimental conditions and timescales described here reports an average of up and down transitions that cannot be resolved.

In summary, our results localize the impacts of mutations on conformational dynamics to two specific loci: the trimer stalk region and NTD. These offer a timeline of variant emergence effects on S trimer conformational dynamics. Every successive variant S protein displays a progressive reduction in dynamics at a central stalk region in the S2 subunit and progressive increases in dynamics in NTD and RBD. The increased stability conferred by the D614G S substitution formed the basis for further optimization of S conformation through changes in NTD and heptad repeat dynamics that could have advanced overall viral fitness and transmissibility. Alpha S showed no differences at the stalk region but showed increases in NTD and RBD dynamics. Delta S showed more stabilization at the stalk region and decreased NTD dynamics. Omicron BA.1 S showed even greater stabilization of the stalk region together with increased NTD and RBD dynamics. Overall, these results suggest that while near-maximal trimer stalk stability

has been achieved, emerging variants continue to show progressive increases in NTD and RBD dynamics. It remains to be seen how progressive changes in stalk stabilization and enhanced NTD dynamics impact neutralization of emergent variants by antibodies generated against wild-type S.

Changes in stabilization and dynamics resulting from specific spike mutations detail the evolutionary trajectory of spike protein in emerging variants. This provides a basis for progressively enhanced viral fitness and carries major implications for spike evolution and neutralization.

Materials and Methods

Expression and purification of SARS-CoV-2 S proteins

Expression and purification of SARS-CoV-2 S ectodomains were performed as previously described (Barnes, Jette, et al., 2020; Barnes, West, et al., 2020). SARS-CoV-2 S constructs were composed of residues 16–1206 of the early SARS-CoV-2 isolate (GenBank MN985325.1), Alpha variant (GISAID EPI_ISL_601443), Delta variant (GenBank QWK65230.1), or Omicron variant (BA.1) (GISAID EPI_ISL_9845731) with the following stabilizing mutations: 2P (Pallesen et al., 2017) or 6P (Hsieh et al., 2020), the furin cleavage site mutated to Ala, a C-terminal TEV protease site (GSG-RENLYFQG), foldon trimerization motif (GGGSG-YIPEAPRDGQAYVRKDGEWVLLSTFL), 8x-His tag (G-HHHHHHHH), and AviTag (GLNDIFEAQKIEWHE). All S constructs were expressed using the Expi293T transient transfections system (GIBCO). S trimers from clarified transfected cell supernatants were purified over HisTrap High Performance columns (Cytiva), followed by size-exclusion chromatography (SEC) using a Superose 6 increase 10 300 column (Cytiva). Fractions corresponding to S trimers were collected and concentrated in 10% glycerol TBS (20 mM Tris, 150 mM NaCl, pH 8.0) then

595 flash frozen in liquid nitrogen and stored at -80 ºC. Downstream purification was completed within
596 12 h of the transfected cell harvest to maximize the quality of trimeric, well-folded S trimers.
597
598 **Bottom-up proteomics and glycan profiling**
599 Recombinant S protein variants were digested with trypsin overnight. Samples were
600 separated by RP-HPLC using a Thermo Scientific EASY-nLC™ 1200 UPLC system connected
601 to a Thermo Scientific™ PepMap C18 column, 15 cm × 75 µm over a 90 min 5-25%, 15 min from
602 40-95 % gradient (A: water, 0.1% formic acid; B: 80 % acetonitrile, 0.1% formic acid) at 300
603 nL/min flow rate. The samples were analyzed on the Thermo Scientific™ Orbitrap Eclipse™
604 Tribrid™ mass spectrometer using DDA FT HCD MS2 method. FT MS1 was acquired at
605 resolution settings of 120K at m/z 200 and FTMS2 at resolution of 30K at m/z 200.
606 The Thermo Scientific™ Proteome Discoverer™ 2.5 software with the Byonic™ search node
607 (Protein Metrics) were used for glycopeptide data analysis and glycoform quantification. Data
608 were searched against a database containing the Uniprot/SwissProt entries of the model proteins
609 with/out common contaminants and 57 human plasma glycans with a 1% FDR criteria for protein
610 spectral matches. The peptide spectra were also manually validated to confirm identification of
611 glycosylation sites.
612
613 **Deuterium exchange**
614 Labeling buffer was prepared by diluting 20X PBS in H_2O in D_2O (99.9%). 3 µL of sample
615 were added to 57 µL of labeling buffer for a final labeling concentration of 90.16%. Deuterium
616 labelling was carried out for 1, 2, 10, 30, and 100 min at 20ºC using a PAL-RTC (Leap)
617 autosampler. During automated HDXMS experiments protein samples were stored at 0 degrees

618 and stability was assessed by staggering technical replicates. After labelling, equivalent volumes
619 of labeling reaction and prechilled quench solution (1.5 M GndHCl, 0.25 M TCEP) was added to
620 bring the reaction to pH 2.5.
621
622 **Mass spectrometry and peptide identification**
623 Approximately 8-10 pmol of sample were loaded onto a BEH pepsin column (2.1 x 30
624 mm) (Waters, Milford, MA) in 0.1% formic acid at 75 µL/min. Proteolyzed peptides were trapped
625 in a C18 trap column (ACQUITY BEH C18 VanGuard Pre-column, 1.7 µM, Waters, Milford,
626 MA). Peptides were eluted in an acetonitrile gradient (8-40%) in 0.1% formic acid on a reverse
627 phase C18 column (AQUITY UPLC BEH C18 Column, Waters, Milford, MA) at 40 µL/min. All
628 fluidics were controlled by nanoACQUITY Binary Solvent Manager (Waters, Milford, MA).
629 Electrospray ionization mode was utilized and ionized peptides were sprayed onto a SYNAPT XS
630 mass spectrometer (Waters, Milford, MA) acquired in $HDMS^E$ Mode. Ion mobility settings of 600
631 m/s wave velocity and 197 m/s transfer wave velocity were used with collision energies of 4 and
632 2 V were used for trap and transfer, respectively. High collision energy was ramped from 20 to 45
633 V while a 25 V cone voltage was used to obtain mass spectra ranging from 50-2000 Da (10 min)
634 in positive ion mode. A flow rate of 5 µL/min was used to inject 100 fmol/µL of [Glu^1]-
635 fibrinopeptide B ([Glu^1]-Fib) as lockspray reference mass.
636 Peptides of wild-type and SARS CoV-2 variant S proteins were identified through
637 independent searches of mass spectra from the undeuterated samples in two steps. First, peptides
638 common to wild-type and variant S proteins were identified from a database containing the amino
639 acid sequence of wild-type and D614G S using PROTEIN LYNX GLOBAL SERVER version 3.0
640 (Waters, Milford, MA) software in $HDMS^E$ mode for non-specific protease cleavage. Search

parameters in PLGS were set to 'no fixed or variable modifier reagents' and variable N-linked glycosylation.

Deuterium exchange was quantitated using DynamX v3.0 (Waters, Milford, MA) with cutoff filters of: minimum intensity = 2000, minimum peptide length = 4, maximum peptide length = 25, minimum products per amino acid = 0.2, and precursor ion error tolerance <10 ppm. Three undeuterated replicates were collected for wild-type and variant S proteins, and the final peptide list includes only peptides that fulfilled the above-described criteria and were identified independently in at least 2 of the 3 undeuterated samples.

In the second step, the workflow was repeated to identify peptides unique to S protein variants. Pepsin fragment peptides from each variant S protein were identified from a database containing the amino acid sequence of the corresponding variant S. Deuterium exchange in these peptides were analyzed using DynamX 3.0 with identical parameters described above.

Hydrogen-Deuterium Exchange Analysis

The average number of deuterons exchanged in each peptide was calculated by subtracting the centroid mass of the undeuterated reference spectra from each deuterated spectra. Peptides were independently analyzed for quality across technical replicates. Relative deuterium exchange and difference plots were generated by DynamX v3.0. Relative deuterium exchange plots are reported as RFU which is the ratio of exchanged deuterons to possible exchange deuterons. Back exchange estimates were determined by RFU values from a 24 h labeling experiment and are shown in Figure 3-figure supplement 5. Deuteros (Lau et al., 2021) was used to generate Woods plots using a peptide level significance test ($p<0.01$). The mass spectrometry proteomics data will be deposited to the ProteomeXchange Consortium via the PRIDE partner repository.

Acknowledgments

Funding:

Startup funding from the Pennsylvania State University (PSU) to GSA.

We thank Rosa Viner (Thermo Scientific, San Jose, CA) for spike protein glycan analysis.

Competing interests: All authors declare they have no competing interest.

Data and Materials availability:

Mass Spectrometry data: ProteomeXchange Consortium via the PRIDE partner repository

All data is available in the main text and supplemental information.

Information on recombinant proteins and reagents is available upon request

References

Aleem, A., Akbar Samad, A. B., & Slenker, A. K. (2022). Emerging Variants of SARS-CoV-2 And Novel Therapeutics Against Coronavirus (COVID-19). In *StatPearls*. StatPearls Publishing. http://www.ncbi.nlm.nih.gov/books/NBK570580/

files/774/NBK570580.html

http://www.ncbi.nlm.nih.gov/pubmed/34033342

Amanat, F., Strohmeier, S., Rathnasinghe, R., Schotsaert, M., Coughlan, L., Garcia-Sastre, A., & Krammer, F. (2021). Introduction of Two Prolines and Removal of the Polybasic Cleavage Site Lead to Higher Efficacy of a Recombinant Spike-Based SARS-CoV-2 Vaccine in the Mouse Model. *mBio*, *12*(2). https://doi.org/10.1128/mBio.02648-20

Araf, Y., Akter, F., Tang, Y. D., Fatemi, R., Parvez, M. S. A., Zheng, C., & Hossain, M. G. (2022). Omicron variant of SARS-CoV-2: Genomics, transmissibility, and responses to current COVID-19 vaccines. *J Med Virol*, *94*(5), 1825-1832. https://doi.org/10.1002/jmv.27588

Barnes, C. O., Jette, C. A., Abernathy, M. E., Dam, K. A., Esswein, S. R., Gristick, H. B., Malyutin, A. G., Sharaf, N. G., Huey-Tubman, K. E., Lee, Y. E., Robbiani, D. F., Nussenzweig, M. C., West, A. P., Jr., & Bjorkman, P. J. (2020). SARS-CoV-2 neutralizing antibody structures inform therapeutic strategies. *Nature*, *588*(7839), 682-687. https://doi.org/10.1038/s41586-020-2852-1

Barnes, C. O., West, A. P., Jr., Huey-Tubman, K. E., Hoffmann, M. A. G., Sharaf, N. G., Hoffman, P. R., Koranda, N., Gristick, H. B., Gaebler, C., Muecksch, F., Lorenzi, J. C. C., Finkin, S., Hagglof, T., Hurley, A., Millard, K. G., Weisblum, Y., Schmidt, F., Hatziioannou, T., Bieniasz, P. D., . . . Bjorkman, P. J. (2020). Structures of Human Antibodies Bound to SARS-CoV-2 Spike Reveal Common Epitopes and Recurrent Features of Antibodies. *Cell*, *182*(4), 828-842 e816. https://doi.org/10.1016/j.cell.2020.06.025

Cai, Y., Zhang, J., Xiao, T., Peng, H., Sterling, S. M., Walsh, R. M., Jr., Rawson, S., Rits-Volloch, S., & Chen, B. (2020). Distinct conformational states of SARS-CoV-2 spike protein. *Science*, *369*(6511), 1586-1592. https://doi.org/10.1126/science.abd4251

Chang, T. J., Yang, D. M., Wang, M. L., Liang, K. H., Tsai, P. H., Chiou, S. H., Lin, T. H., & Wang, C. T. (2020). Genomic analysis and comparative multiple sequences of SARS-CoV2. *J Chin Med Assoc*, *83*(6), 537-543. https://doi.org/10.1097/JCMA.0000000000000335

Corman, V. M., Muth, D., Niemeyer, D., & Drosten, C. (2018). Chapter Eight - Hosts and Sources of Endemic Human Coronaviruses. In M. Kielian, T. C. Mettenleiter, & M. J. Roossinck (Eds.), *Advances in Virus Research* (Vol. 100, pp. 163-188). Academic Press. https://www.sciencedirect.com/science/article/pii/S0065352718300010

files/788/S0065352718300010.html

Costello, S. M., Shoemaker, S. R., Hobbs, H. T., Nguyen, A. W., Hsieh, C.-L., Maynard, J. A., McLellan, J. S., Pak, J. E., & Marqusee, S. (2022). The SARS-CoV-2 spike reversibly samples an open-trimer conformation exposing novel epitopes. *Nature Structural & Molecular Biology*, *29*(3), 229-238. https://doi.org/10.1038/s41594-022-00735-5

745 Derking, R., & Sanders, R. W. (2021). Structure-guided envelope trimer design in HIV-1 vaccine
746 development: a narrative review. *J Int AIDS Soc*, *24 Suppl 7*, e25797.
747 https://doi.org/10.1002/jia2.25797
748 Duan, L., Zheng, Q., Zhang, H., Niu, Y., Lou, Y., & Wang, H. (2020). The SARS-CoV-2 Spike
749 Glycoprotein Biosynthesis, Structure, Function, and Antigenicity: Implications for the
750 Design of Spike-Based Vaccine Immunogens. *Front Immunol*, *11*, 576622.
751 https://doi.org/10.3389/fimmu.2020.576622
752 Edwards, R. J., Mansouri, K., Stalls, V., Manne, K., Watts, B., Parks, R., Janowska, K., Gobeil,
753 S. M. C., Kopp, M., Li, D., Lu, X., Mu, Z., Deyton, M., Oguin, T. H., Sprenz, J.,
754 Williams, W., Saunders, K. O., Montefiori, D., Sempowski, G. D., . . . Acharya, P.
755 (2021). Cold sensitivity of the SARS-CoV-2 spike ectodomain. *Nature Structural &*
756 *Molecular Biology*, *28*(2), 128-131. https://doi.org/10.1038/s41594-020-00547-5
757 Englander, S. W., & Kallenbach, N. R. (1983). Hydrogen exchange and structural dynamics of
758 proteins and nucleic acids. *Q Rev Biophys*, *16*(4), 521-655.
759 https://doi.org/10.1017/s0033583500005217
760 Gobeil, S. M., Janowska, K., McDowell, S., Mansouri, K., Parks, R., Manne, K., Stalls, V.,
761 Kopp, M. F., Henderson, R., Edwards, R. J., Haynes, B. F., & Acharya, P. (2021).
762 D614G Mutation Alters SARS-CoV-2 Spike Conformation and Enhances Protease
763 Cleavage at the S1/S2 Junction. *Cell Rep*, *34*(2), 108630.
764 https://doi.org/10.1016/j.celrep.2020.108630
765 Han, P., Li, L., Liu, S., Wang, Q., Zhang, D., Xu, Z., Han, P., Li, X., Peng, Q., Su, C., Huang, B.,
766 Li, D., Zhang, R., Tian, M., Fu, L., Gao, Y., Zhao, X., Liu, K., Qi, J., . . . Wang, P.
767 (2022). Receptor binding and complex structures of human ACE2 to spike RBD from
768 omicron and delta SARS-CoV-2. *Cell*, *185*(4), 630-640.e610.
769 https://doi.org/10.1016/j.cell.2022.01.001
770 Hodge, E. A., Benhaim, M. A., & Lee, K. K. (2020). Bridging protein structure, dynamics, and
771 function using hydrogen/deuterium-exchange mass spectrometry. *Protein Sci*, *29*(4), 843-
772 855. https://doi.org/10.1002/pro.3790
773 Hoofnagle, A. N., Resing, K. A., & Ahn, N. G. (2003). Protein analysis by hydrogen exchange
774 mass spectrometry. *Annu Rev Biophys Biomol Struct*, *32*, 1-25.
775 https://doi.org/10.1146/annurev.biophys.32.110601.142417
776 Hsieh, C.-L., Goldsmith, J. A., Schaub, J. M., DiVenere, A. M., Kuo, H.-C., Javanmardi, K., Le,
777 K. C., Wrapp, D., Lee, A. G., Liu, Y., Chou, C.-W., Byrne, P. O., Hjorth, C. K., Johnson,
778 N. V., Ludes-Meyers, J., Nguyen, A. W., Park, J., Wang, N., Amengor, D., . . . McLellan,
779 J. S. (2020). Structure-based design of prefusion-stabilized SARS-CoV-2 spikes. *Science*,
780 *369*(6510), 1501-1505. https://doi.org/10.1126/science.abd0826
781 Hsieh, S. M., Liu, M. C., Chen, Y. H., Lee, W. S., Hwang, S. J., Cheng, S. H., Ko, W. C.,
782 Hwang, K. P., Wang, N. C., Lee, Y. L., Lin, Y. L., Shih, S. R., Huang, C. G., Liao, C. C.,
783 Liang, J. J., Chang, C. S., Chen, C., Lien, C. E., Tai, I. C., & Lin, T. Y. (2021). Safety
784 and immunogenicity of CpG 1018 and aluminium hydroxide-adjuvanted SARS-CoV-2 S-
785 2P protein vaccine MVC-COV1901: interim results of a large-scale, double-blind,
786 randomised, placebo-controlled phase 2 trial in Taiwan. *Lancet Respir Med*, *9*(12), 1396-
787 1406. https://doi.org/10.1016/S2213-2600(21)00402-1
788 Kaltashov, I. A., & Eyles, S. J. (2002). Crossing the phase boundary to study protein dynamics
789 and function: combination of amide hydrogen exchange in solution and ion fragmentation
790 in the gas phase. *J Mass Spectrom*, *37*(6), 557-565. https://doi.org/10.1002/jms.338

Ke, Z., Oton, J., Qu, K., Cortese, M., Zila, V., McKeane, L., Nakane, T., Zivanov, J., Neufeldt, C. J., Cerikan, B., Lu, J. M., Peukes, J., Xiong, X., Krausslich, H. G., Scheres, S. H. W., Bartenschlager, R., & Briggs, J. A. G. (2020). Structures and distributions of SARS-CoV-2 spike proteins on intact virions. *Nature*, *588*(7838), 498-502. https://doi.org/10.1038/s41586-020-2665-2

Kirchdoerfer, R. N., Wang, N., Pallesen, J., Wrapp, D., Turner, H. L., Cottrell, C. A., Corbett, K. S., Graham, B. S., McLellan, J. S., & Ward, A. B. (2018). Publisher Correction: Stabilized coronavirus spikes are resistant to conformational changes induced by receptor recognition or proteolysis. *Sci Rep*, *8*(1), 17823. https://doi.org/10.1038/s41598-018-36918-8

Lan, J., Ge, J., Yu, J., Shan, S., Zhou, H., Fan, S., Zhang, Q., Shi, X., Wang, Q., Zhang, L., & Wang, X. (2020). Structure of the SARS-CoV-2 spike receptor-binding domain bound to the ACE2 receptor. *Nature*, *581*(7807), 215-220. https://doi.org/10.1038/s41586-020-2180-5

Lau, A. M., Claesen, J., Hansen, K., & Politis, A. (2021). Deuteros 2.0: peptide-level significance testing of data from hydrogen deuterium exchange mass spectrometry. *Bioinformatics*, *37*(2), 270-272. https://doi.org/10.1093/bioinformatics/btaa677

Lien, C. E., Kuo, T. Y., Lin, Y. J., Lian, W. C., Lin, M. Y., Liu, L. T., Cheng, J., Chou, Y. C., & Chen, C. (2021). Evaluating the Neutralizing Ability of a CpG-Adjuvanted S-2P Subunit Vaccine Against Severe Acute Respiratory Syndrome Coronavirus 2 (SARS-CoV-2) Variants of Concern. *Clin Infect Dis*. https://doi.org/10.1093/cid/ciab711

Lien, C. E., Lin, Y. J., Chen, C., Lian, W. C., Kuo, T. Y., Campbell, J. D., Traquina, P., Lin, M. Y., Liu, L. T., Chuang, Y. S., Ko, H. Y., Liao, C. C., Chen, Y. H., Jan, J. T., Ma, H. H., Sun, C. P., Lin, Y. S., Wu, P. Y., Wang, Y. C., . . . Lin, Y. L. (2021). CpG-adjuvanted stable prefusion SARS-CoV-2 spike protein protected hamsters from SARS-CoV-2 challenge. *Sci Rep*, *11*(1), 8761. https://doi.org/10.1038/s41598-021-88283-8

Lim, X.-X., Chandramohan, A., Lim, X.-Y. E., Crowe, J. E., Lok, S.-M., & Anand, G. S. (2017). Epitope and Paratope Mapping Reveals Temperature-Dependent Alterations in the Dengue-Antibody Interface. *Structure*, *25*(9), 1391-1402.e1393. https://doi.org/10.1016/j.str.2017.07.007

Lim, X. X., Chandramohan, A., Lim, X. Y., Bag, N., Sharma, K. K., Wirawan, M., Wohland, T., Lok, S. M., & Anand, G. S. (2017). Conformational changes in intact dengue virus reveal serotype-specific expansion. *Nat Commun*, *8*, 14339. https://doi.org/10.1038/ncomms14339

Liu, L., Iketani, S., Guo, Y., Chan, J. F. W., Wang, M., Liu, L., Luo, Y., Chu, H., Huang, Y., Nair, M. S., Yu, J., Chik, K. K. H., Yuen, T. T. T., Yoon, C., To, K. K. W., Chen, H., Yin, M. T., Sobieszczyk, M. E., Huang, Y., . . . Ho, D. D. (2022). Striking antibody evasion manifested by the Omicron variant of SARS-CoV-2. *Nature*, *602*(7898), 676-681. https://doi.org/10.1038/s41586-021-04388-0

Liu, Y., Liu, J., Johnson, B. A., Xia, H., Ku, Z., Schindewolf, C., Widen, S. G., An, Z., Weaver, S. C., Menachery, V. D., Xie, X., & Shi, P.-Y. (2022). Delta spike P681R mutation enhances SARS-CoV-2 fitness over Alpha variant. *Cell Reports*, 110829. https://doi.org/10.1016/j.celrep.2022.110829

Martinez-Flores, D., Zepeda-Cervantes, J., Cruz-Resendiz, A., Aguirre-Sampieri, S., Sampieri, A., & Vaca, L. (2021). SARS-CoV-2 Vaccines Based on the Spike Glycoprotein and

836 Implications of New Viral Variants. *Frontiers in Immunology*, *12*. https://doi.org/ARTN
837 701501

838 10.3389/fimmu.2021.701501
839 Narang, D., James, D. A., Balmer, M. T., & Wilson, D. J. (2021). Protein Footprinting,
840 Conformational Dynamics, and Core Interface-Adjacent Neutralization "Hotspots" in the
841 SARS-CoV-2 Spike Protein Receptor Binding Domain/Human ACE2 Interaction.
842 *Journal of the American Society for Mass Spectrometry*, *32*(7), 1593-1600.
843 https://doi.org/10.1021/jasms.0c00465
844 Oganesyan, I., Lento, C., & Wilson, D. J. (2018). Contemporary hydrogen deuterium exchange
845 mass spectrometry. *Methods*, *144*, 27-42. https://doi.org/10.1016/j.ymeth.2018.04.023
846 Ozono, S., Zhang, Y., Ode, H., Sano, K., Tan, T. S., Imai, K., Miyoshi, K., Kishigami, S., Ueno,
847 T., Iwatani, Y., Suzuki, T., & Tokunaga, K. (2021). SARS-CoV-2 D614G spike mutation
848 increases entry efficiency with enhanced ACE2-binding affinity. *Nature*
849 *Communications*, *12*(1), 848. https://doi.org/10.1038/s41467-021-21118-2
850 Pallesen, J., Wang, N., Corbett, K. S., Wrapp, D., Kirchdoerfer, R. N., Turner, H. L., Cottrell, C.
851 A., Becker, M. M., Wang, L., Shi, W., Kong, W. P., Andres, E. L., Kettenbach, A. N.,
852 Denison, M. R., Chappell, J. D., Graham, B. S., Ward, A. B., & McLellan, J. S. (2017).
853 Immunogenicity and structures of a rationally designed prefusion MERS-CoV spike
854 antigen. *Proc Natl Acad Sci U S A*, *114*(35), E7348-E7357.
855 https://doi.org/10.1073/pnas.1707304114
856 Pandey, U., Yee, R., Shen, L., Judkins, A. R., Bootwalla, M., Ryutov, A., Maglinte, D. T.,
857 Ostrow, D., Precit, M., Biegel, J. A., Bender, J. M., Gai, X., & Dien Bard, J. (2021). High
858 Prevalence of SARS-CoV-2 Genetic Variation and D614G Mutation in Pediatric Patients
859 With COVID-19. *Open Forum Infect Dis*, *8*(6), ofaa551.
860 https://doi.org/10.1093/ofid/ofaa551
861 Peacock, R. B., Davis, J. R., Markwick, P. R. L., & Komives, E. A. (2018). Dynamic
862 Consequences of Mutation of Tryptophan 215 in Thrombin. *Biochemistry*, *57*(18), 2694-
863 2703. https://doi.org/10.1021/acs.biochem.8b00262
864 Peacock, T. P., Goldhill, D. H., Zhou, J., Baillon, L., Frise, R., Swann, O. C., Kugathasan, R.,
865 Penn, R., Brown, J. C., Sanchez-David, R. Y., Braga, L., Williamson, M. K., Hassard, J.
866 A., Staller, E., Hanley, B., Osborn, M., Giacca, M., Davidson, A. D., Matthews, D. A., &
867 Barclay, W. S. (2021). The furin cleavage site in the SARS-CoV-2 spike protein is
868 required for transmission in ferrets. *Nat Microbiol*, *6*(7), 899-909.
869 https://doi.org/10.1038/s41564-021-00908-w
870 Plante, J. A., Liu, Y., Liu, J., Xia, H., Johnson, B. A., Lokugamage, K. G., Zhang, X., Muruato,
871 A. E., Zou, J., Fontes-Garfias, C. R., Mirchandani, D., Scharton, D., Bilello, J. P., Ku, Z.,
872 An, Z., Kalveram, B., Freiberg, A. N., Menachery, V. D., Xie, X., . . . Shi, P. Y. (2021).
873 Spike mutation D614G alters SARS-CoV-2 fitness. *Nature*, *592*(7852), 116-121.
874 https://doi.org/10.1038/s41586-020-2895-3
875 Privalov, P. L. (1990). Cold denaturation of proteins. *Crit Rev Biochem Mol Biol*, *25*(4), 281-
876 305. https://doi.org/10.3109/10409239009090612
877 Qing, E., Kicmal, T., Kumar, B., Hawkins, G. M., Timm, E., Perlman, S., & Gallagher, T.
878 (2021). Dynamics of SARS-CoV-2 Spike Proteins in Cell Entry: Control Elements in the
879 Amino-Terminal Domains. *mBio*, *12*(4), e0159021. https://doi.org/10.1128/mBio.01590-
880 21

Raghuvamsi, P. V., Tulsian, N. K., Samsudin, F., Qian, X., Purushotorman, K., Yue, G., Kozma, M. M., Hwa, W. Y., Lescar, J., Bond, P. J., MacAry, P. A., & Anand, G. S. (2021). SARS-CoV-2 S protein:ACE2 interaction reveals novel allosteric targets. *Elife*, *10*. https://doi.org/10.7554/eLife.63646

Saito, A., Irie, T., Suzuki, R., Maemura, T., Nasser, H., Uriu, K., Kosugi, Y., Shirakawa, K., Sadamasu, K., Kimura, I., Ito, J., Wu, J., Iwatsuki-Horimoto, K., Ito, M., Yamayoshi, S., Ozono, S., Butlertanaka, E. P., Tanaka, Y. L., Shimizu, R., . . . Sato, K. (2021). *SARS-CoV-2 spike P681R mutation, a hallmark of the Delta variant, enhances viral fusogenicity and pathogenicity*. https://www.biorxiv.org/content/10.1101/2021.06.17.448820v2

files/781/2021.06.17.448820v2.html

Shang, J., Wan, Y., Luo, C., Ye, G., Geng, Q., Auerbach, A., & Li, F. (2020). Cell entry mechanisms of SARS-CoV-2. *Proc Natl Acad Sci U S A*, *117*(21), 11727-11734. https://doi.org/10.1073/pnas.2003138117

Tian, D., Sun, Y., Zhou, J., & Ye, Q. (2021). The Global Epidemic of the SARS-CoV-2 Delta Variant, Key Spike Mutations and Immune Escape. *Frontiers in Immunology*, *12*, 751778. https://doi.org/10.3389/fimmu.2021.751778

Ulrich, L., Halwe, N. J., Taddeo, A., Ebert, N., Schon, J., Devisme, C., Trueb, B. S., Hoffmann, B., Wider, M., Fan, X., Bekliz, M., Essaidi-Laziosi, M., Schmidt, M. L., Niemeyer, D., Corman, V. M., Kraft, A., Godel, A., Laloli, L., Kelly, J. N., . . . Benarafa, C. (2022). Enhanced fitness of SARS-CoV-2 variant of concern Alpha but not Beta. *Nature*, *602*(7896), 307-313. https://doi.org/10.1038/s41586-021-04342-0

Vankadari, N. (2020). Structure of Furin Protease Binding to SARS-CoV-2 Spike Glycoprotein and Implications for Potential Targets and Virulence. *J Phys Chem Lett*, *11*(16), 6655-6663. https://doi.org/10.1021/acs.jpclett.0c01698

Walls, A. C., Park, Y. J., Tortorici, M. A., Wall, A., McGuire, A. T., & Veesler, D. (2020). Structure, Function, and Antigenicity of the SARS-CoV-2 Spike Glycoprotein. *Cell*, *183*(6), 1735. https://doi.org/10.1016/j.cell.2020.11.032

Wassenaar, T. M., Wanchai, V., Buzard, G., & Ussery, D. W. (2022). The first three waves of the Covid-19 pandemic hint at a limited genetic repertoire for SARS-CoV-2. *FEMS Microbiol Rev*, *46*(3). https://doi.org/10.1093/femsre/fuac003

Watanabe, Y., Allen, J. D., Wrapp, D., McLellan, J. S., & Crispin, M. (2020). Site-specific glycan analysis of the SARS-CoV-2 spike. *Science*, *369*(6501), 330-333. https://doi.org/10.1126/science.abb9983

Weis, D. D., Wales, T. E., Engen, J. R., Hotchko, M., & Ten Eyck, L. F. (2006). Identification and characterization of EX1 kinetics in H/D exchange mass spectrometry by peak width analysis. *J Am Soc Mass Spectrom*, *17*(11), 1498-1509. https://doi.org/10.1016/j.jasms.2006.05.014

Xia, S., Wen, Z., Wang, L., Lan, Q., Jiao, F., Tai, L., Wang, Q., Sun, F., Jiang, S., Lu, L., & Zhu, Y. (2021). Structure-based evidence for the enhanced transmissibility of the dominant SARS-CoV-2 B.1.1.7 variant (Alpha). *Cell Discovery*, *7*(1), 1-5. https://doi.org/10.1038/s41421-021-00349-z

Zhang, J., Cai, Y., Xiao, T., Lu, J., Peng, H., Sterling, S. M., Walsh, R. M., Jr., Rits-Volloch, S., Zhu, H., Woosley, A. N., Yang, W., Sliz, P., & Chen, B. (2021). Structural impact on SARS-CoV-2 spike protein by D614G substitution. *Science*, *372*(6541), 525-530. https://doi.org/10.1126/science.abf2303

Figure 2-figure supplement 1.

Primary sequence coverage for wildtype S 2P versus 6P comparison. Coverage map of wildtype 2P S compared to 6P S using the wildtype 2P sequence showing 160 peptides spanning 53.1% of the S protein. The domain organization of S is also shown.

Figure 2-figure supplement 2.

Primary sequence coverage for wildtype S incubated at 37ºC versus unincubated wildtype S comparison. Coverage map of wildtype S incubated at 37ºC compared to unincubated wildtype S using the wildtype 2P sequence showing 170 peptides spanning 53.3% of the S protein. The domain organization of S is also shown.

941 **Figure 2-figure supplement 3.**

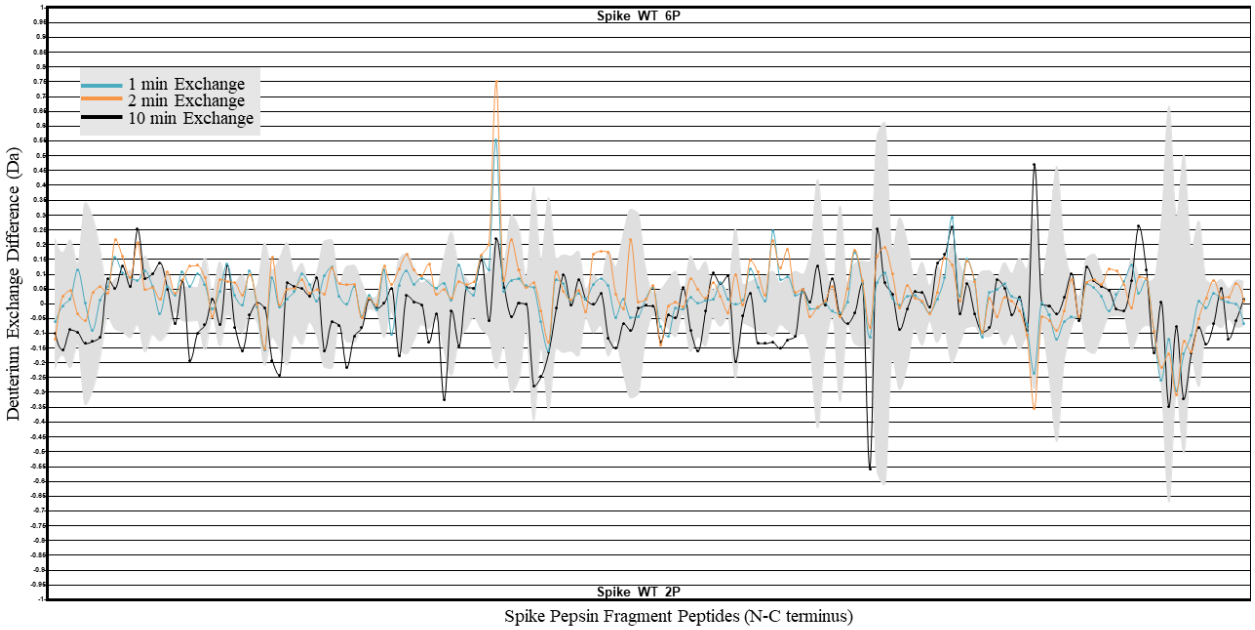

942

943 **HDXMS analysis of 2P and 6P S constructs.** Difference plot of Wildtype 6P S minus Wildtype
944 2P S for peptides N to C terminus. Differences for 1, 2, and 10 min exchange are shown in blue,
945 orange, and black respectively. The grey trace denotes standard errors of deuterium exchange for
946 each peptide.

947

948

949 **Figure 2-figure supplement 4.**

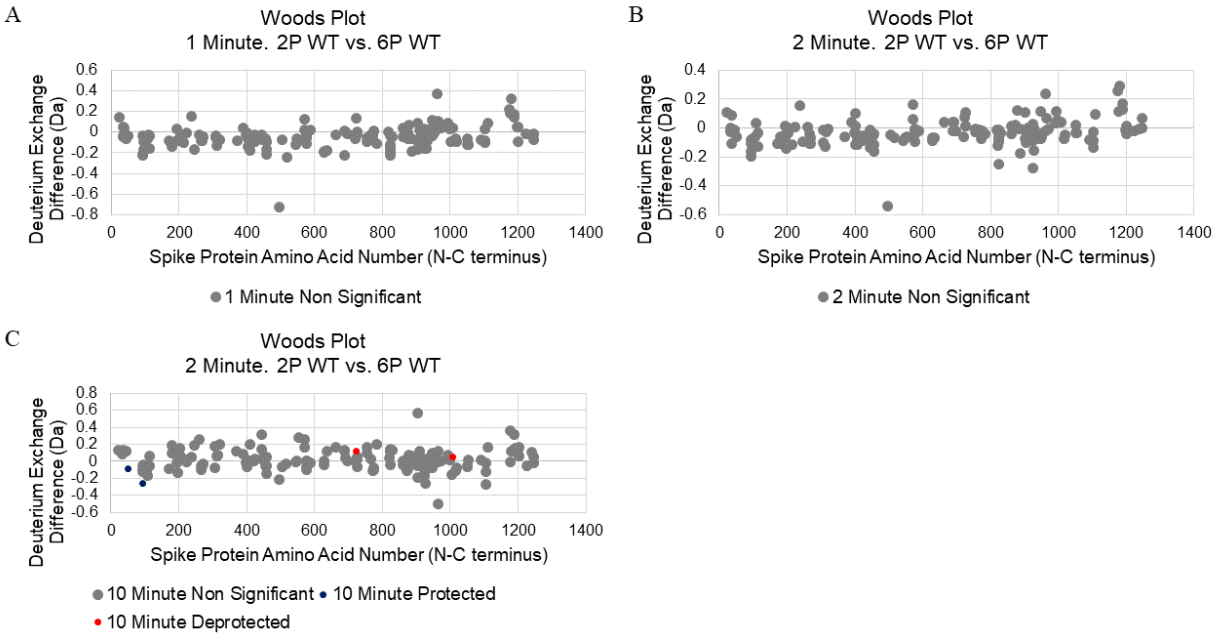

950
951
952 **Woods plot analysis of Wildtype 2P versus 6P S.** Woods plots for 1 min (A), 2 min (B), and
953 10 min (C) exchange. Significantly protected (blue) or deprotected (red) peptides were identified
954 using a peptide level significance test and a P value <0.01.
955
956
957

958 **Figure 2-figure supplement 5.**

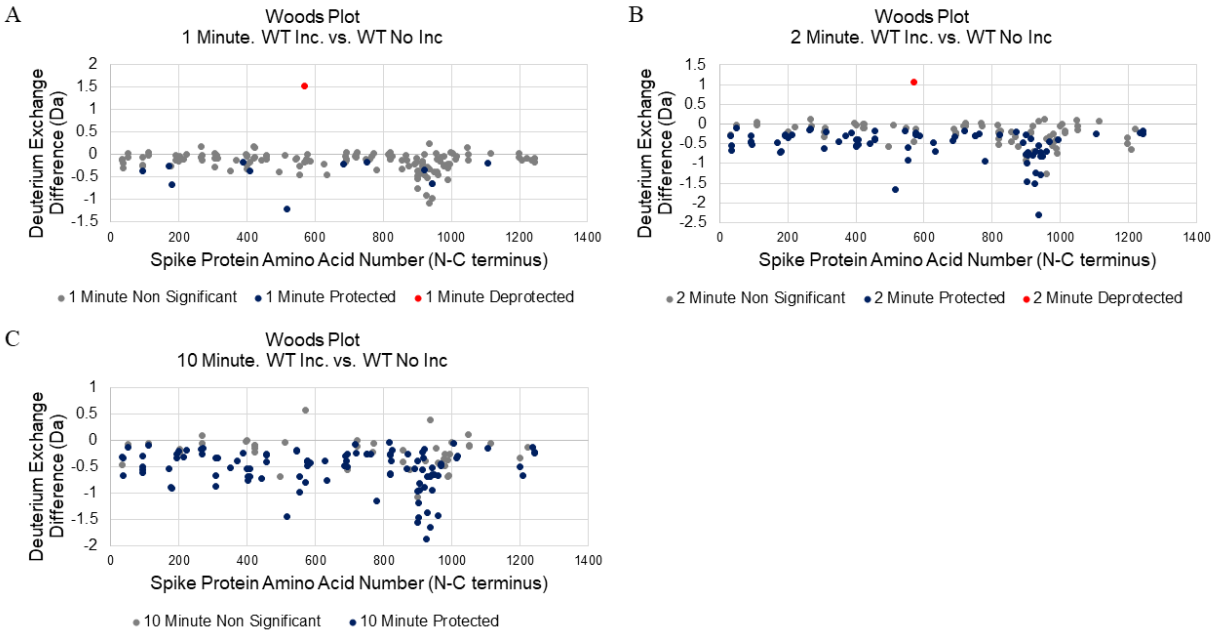

959
960
961 **Woods plot analysis of wildtype S incubated at 37°C versus unincubated wildtype S**. Woods
962 plots for 1 min (A), 2 min (B), and 10 min (C) exchange. Significantly protected (blue) or
963 deprotected (red) peptides were identified using a peptide level significance test and a P value
964 <0.01.
965

966 **Figure 3-figure supplement 1.**

967

968

969 **Primary sequence coverage for D614G S versus wildtype S comparison.** Coverage map of
970 D614G S compared to wildtype S using the Wildtype 2P sequence showing 132 peptides
971 spanning 47.3% of the S protein. The domain organization of S is also shown.

972

Figure 3-figure supplement 2.

Primary sequence coverage for D614G S incubated at 37ºC versus unincubated D614G S comparison. Coverage map of D614G S incubated at 37ºC compared to unincubated D614G S using the D614G 2P sequence showing 133 peptides spanning 48.1% of the S protein. The domain organization of S is also shown.

981 **Figure 3-figure supplement 3**

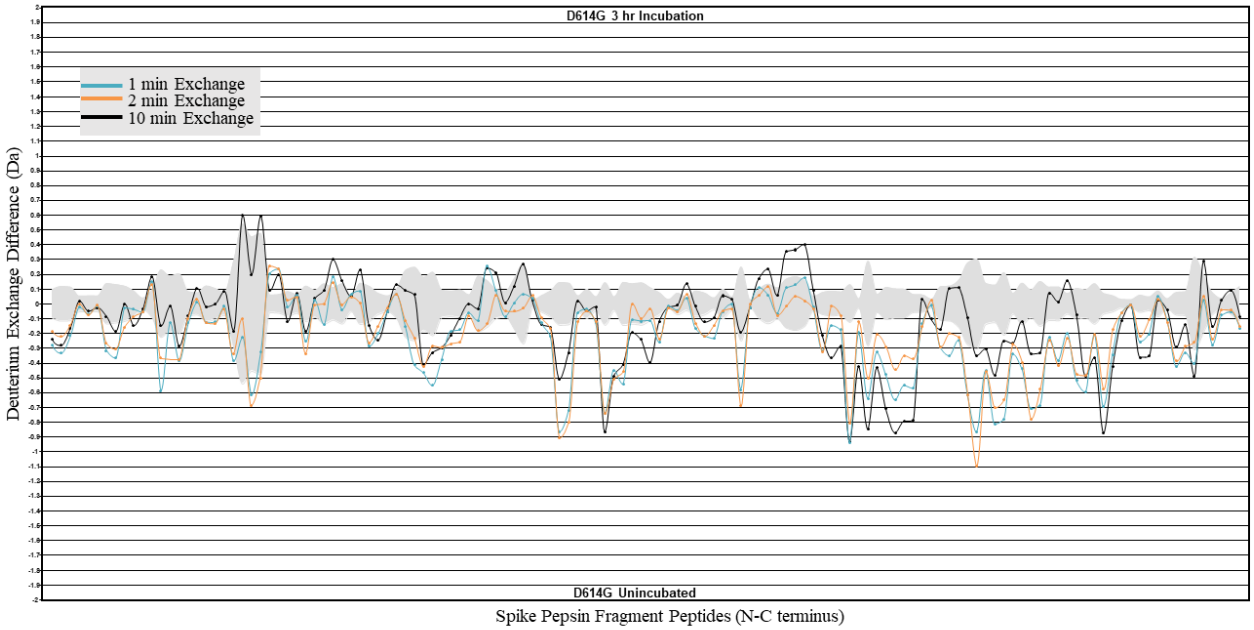

982

983 **HDXMS analysis of incubation effects on D614G S.** Difference plot of D614G S incubated for
984 3 h at 37 ºC minus D614G S with no incubation for peptides N to C terminus. Differences for 1,
985 2, and 10 min exchange are shown in blue, orange, and black respectively. The grey trace
986 denotes standard errors of deuterium exchange for each peptide.

987

988

989 **Figure 3-figure supplement 4**

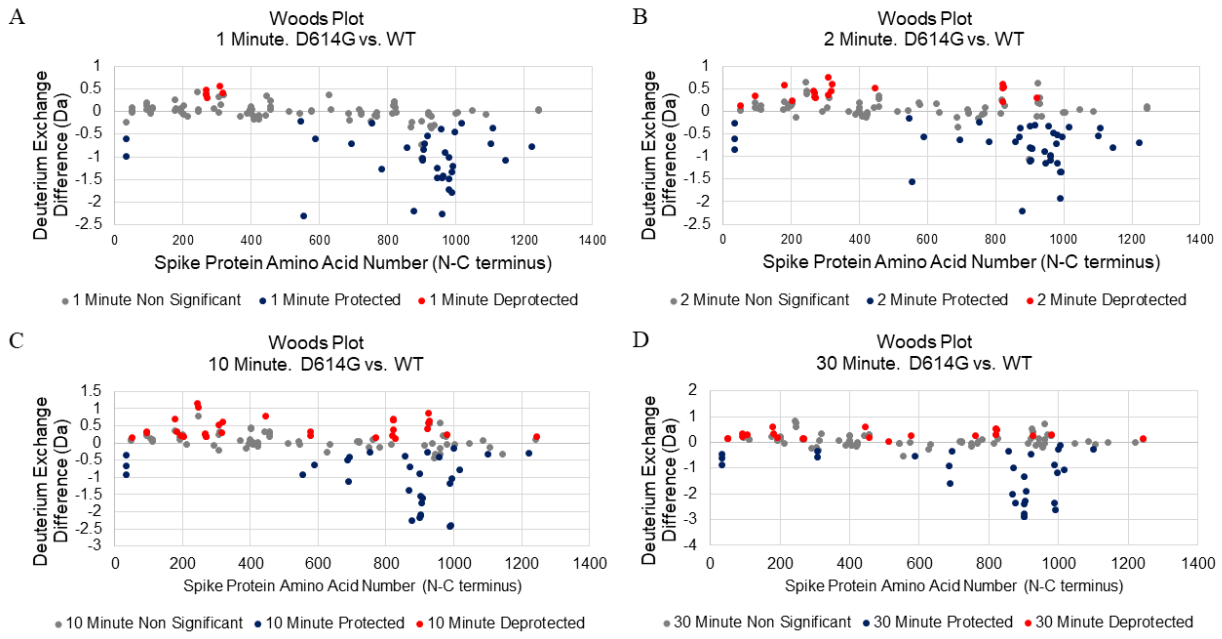

990
991
992 **Woods plot analysis of D614G S versus Wildtype S.** Woods plots for 1 min (A), 2 min (B), 10
993 min (C), and 30 min (D) exchange. Significantly protected (blue) or deprotected (red) peptides
994 were identified using a peptide level significance test and a P value <0.01.
995

996 **Figure 3-figure supplement 5.**

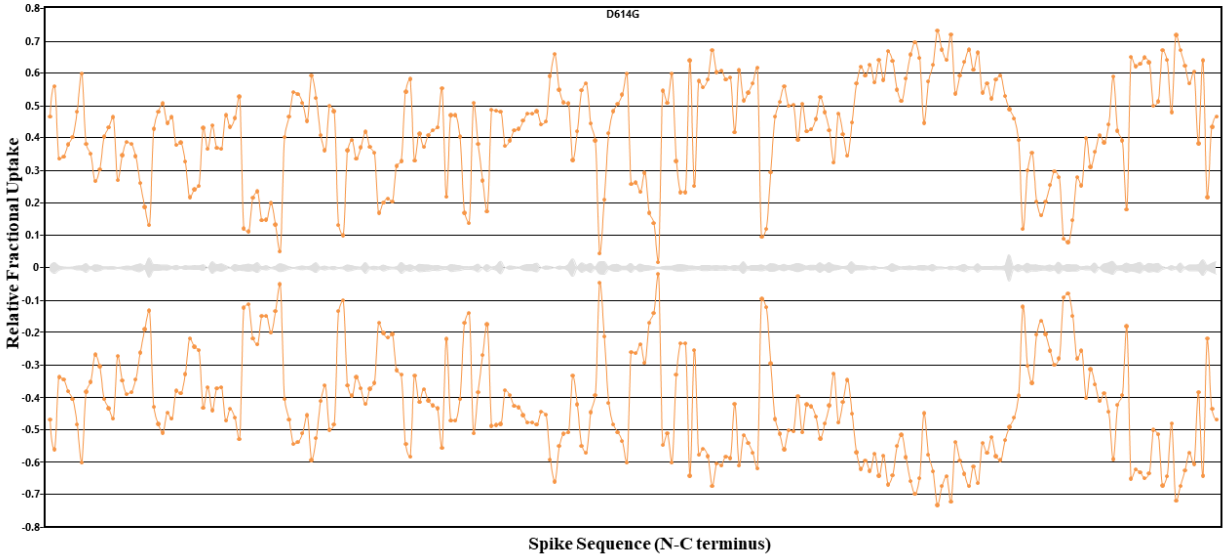

997

998 **Back exchange measurements for pepsin fragment peptides from D614G S.** Deuterium
999 exchange in peptides after long deuteration (Dex = 24 h) is displayed as an RFU plot. The
1000 highest exchanging peptides (943-958 and 957-967) were used to calculate an average back
1001 exchange estimate of 20%.
1002

Figure 4-figure supplement 1.

Primary sequence coverage for Alpha S versus D614G S comparison. Coverage map of Alpha S compared to D614G S using the D614G 2P sequence showing 127 peptides spanning 45.9% of the S protein. The domain organization of S is also shown.

Figure 4-figure supplement 2.

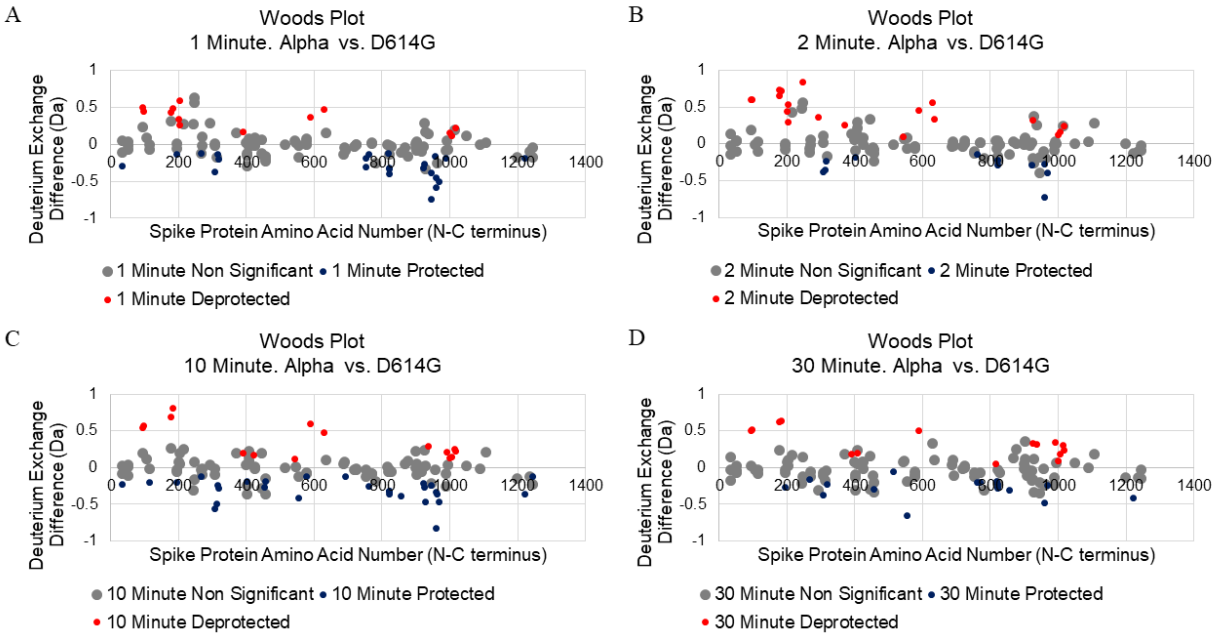

Woods plot analysis of Alpha variant S versus D614G S. Woods plots for 1 min (A), 2 min (B), 10 min (C), and 30 min (D) exchange. Significantly protected (blue) or deprotected (red) peptides were identified using a peptide level significance test and a P value <0.01.

Figure 5-figure supplement 1.

Primary sequence coverage for Delta S versus Alpha S comparison. Coverage map of Delta S compared to Alpha S using the D614G 2P sequence showing 123 peptides spanning 47.0% of the S protein. The domain organization of S is also shown.

1024 **Figure 5-figure supplement 2.**

1025

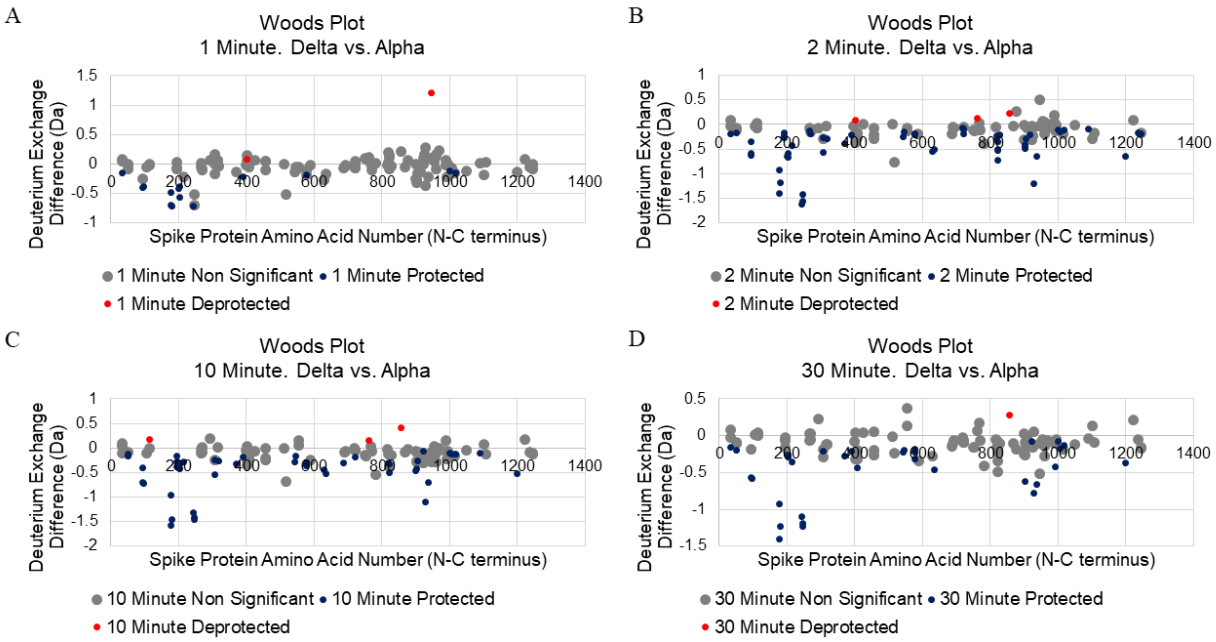

1026
1027

1028 **Woods plot analysis of Delta variant S versus Alpha variant S.** Woods plots for 1 min (A), 2
1029 min (B), 10 min (C), and 30 min (D) exchange. Significantly protected (blue) or deprotected
1030 (red) peptides were identified using a peptide level significance test and a P value <0.01.
1031

Figure 6-figure supplement 1.

Primary sequence coverage for Omicron S versus Delta S comparison. Coverage map of Omicron S compared to Delta S using the D614G 2P sequence showing 96 peptides spanning 36.4% of the S protein. The domain organization of S is also shown.

Figure 6-figure supplement 2.

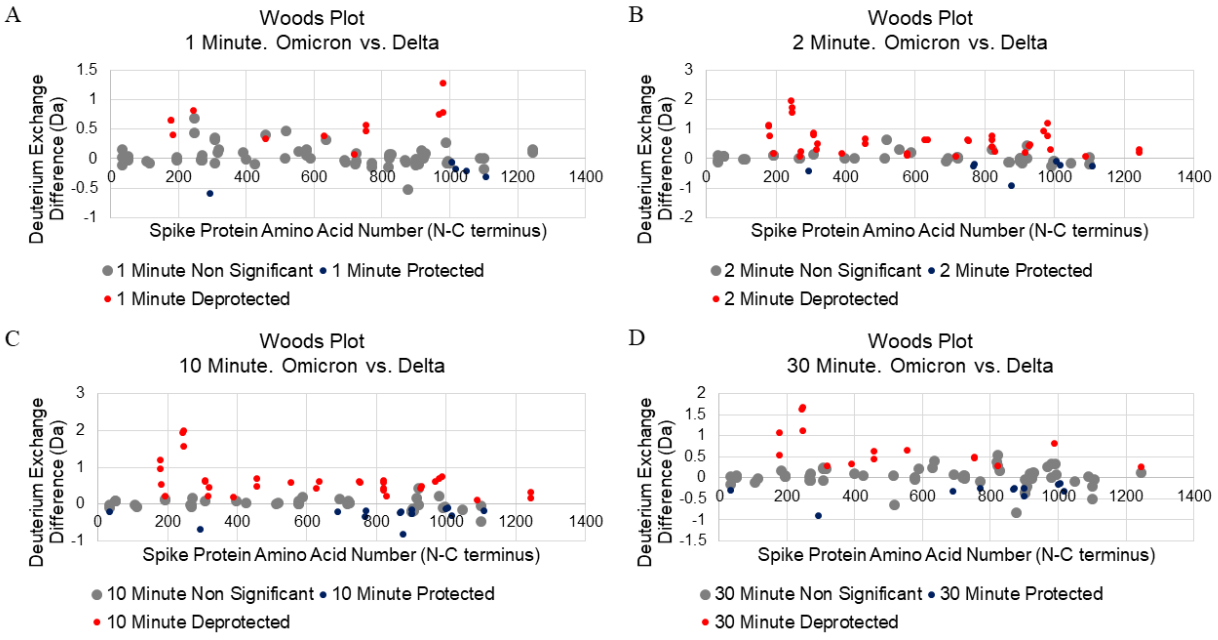

Woods plot analysis of Omicron variant S versus Delta variant S. Woods plots for 1 min (A), 2 min (B), 10 min (C), and 30 min (D) exchange. Significantly protected (blue) or deprotected (red) peptides were identified using a peptide level significance test and a P value <0.01.

Figure 7-figure supplement 1.

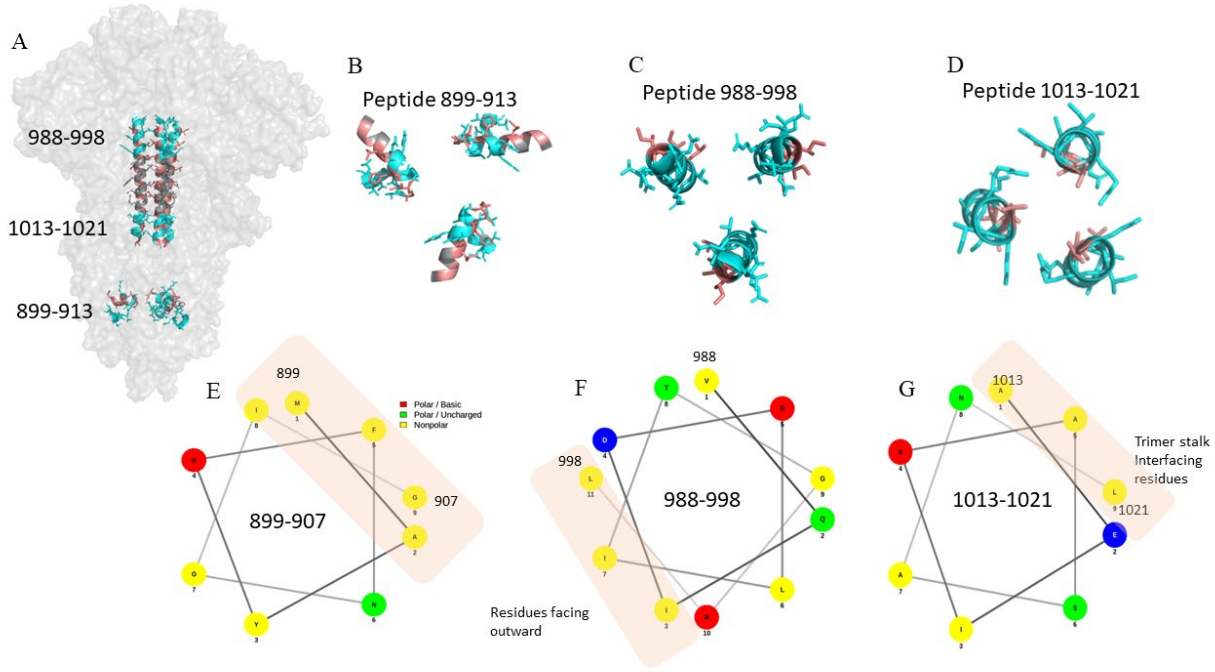

Hydrophobic interactions maintain trimer core at the stalk region (A) Structure of the S trimer highlighting stalk region in salmon (PDB ID: 6VXX). HDXMS analysis peptides at the top, middle and bottom of the trimer stalk are colored cyan. (B, C, D) Cross-sectional view of peptides in the S trimer stalk are colored cyan. Hydrophobic residues are colored salmon. (E, F, G) Helical wheel representation of peptides classifying residues based on polarity. Hydrophobic patches are shown by orange rectangle.

Figure 7-figure supplement 2.

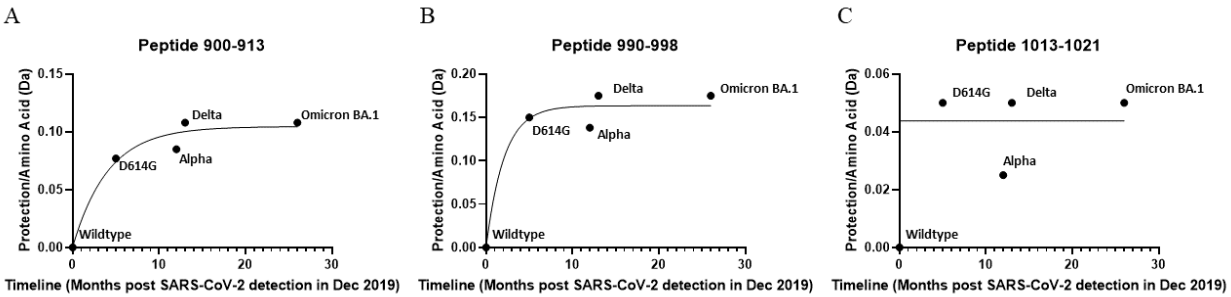

Plot of protection in S trimer stalk peptides as function of timeline of emergence. Protection for each peptide was determined by subtracting deuterium uptake for each variant from wildtype and normalizing to the number of exchangeable amino acids. Protection is plotted against months after the first identification of SARS-CoV-2 in Dec. 2019 and curves fit to a one phase association (Graphpad Prism 3.0, San Diego CA).

Table S1.

	Wildtype		D614G		Delta		Omicron	
	Number of unique glycans detected	Example Glycan	Number of unique glycans detected	Example Glycan	Number of unique glycans detected	Example Glycan	Number of unique glycans detected	Example Glycan
N17	2	HexNAc(4)Hex(6)Fuc(1)NeuAc(1)	3	HexNAc(4)Hex(6)NeuAc(1)	0	N/A	2	HexNAc(5)Hex(4)
N61	40	HexNAc(4)Hex(5)Fuc(1)NeuAc(1)	25	HexNAc(4)Hex(5)NeuAc(2)Na(2)	30	HexNAc(5)Hex(6)NeuAc(1)	12	HexNAc(6)Hex(3)Fuc(1)NeuAc(2)
N74	43	HexNAc(6)Hex(3)Fuc(1)NeuAc(1)	41	HexNAc(4)Hex(5)Fuc(1)NeuAc(2)	40	HexNAc(6)Hex(3)Fuc(1)NeuAc(1)	9	HexNAc(4)Hex(5)Fuc(1)
N122	42	HexNAc(4)Hex(5)Fuc(1)NeuAc(2)Na(1)	41	HexNAc(3)Hex(6)Fuc(1)NeuAc(1)	36	HexNAc(3)Hex(4)NeuAc(1)	39	HexNAc(4)Hex(5)Fuc(1)NeuAc(2)Na(2)
N149	2	HexNAc(2)Hex(5)	2	HexNAc(4)Hex(5)Fuc(1)NeuAc(2)Na(1)	23	HexNAc(3)Hex(6)Fuc(1)NeuAc(1)	0	N/A
N165	6	HexNAc(4)Hex(4)NeuAc(1)Na(1)	7	HexNAc(4)Hex(4)NeuAc(1)Na(1)	25	HexNAc(4)Hex(6)Fuc(1)NeuAc(1)Na(1)	8	HexNAc(4)Hex(4)NeuAc(1)Na(1)
N234	33	HexNAc(4)Hex(6)Fuc(1)NeuAc(1)Na(1)	29	HexNAc(4)Hex(6)Fuc(1)NeuAc(1)	27	HexNAc(4)Hex(5)NeuAc(2)Na(2)	18	HexNAc(4)Hex(6)Fuc(1)NeuAc(1)
N282	7	HexNAc(6)Hex(3)Fuc(1)NeuAc(2)	17	HexNAc(4)Hex(5)Fuc(1)NeuAc(1)Na(1)	11	HexNAc(4)Hex(5)NeuAc(2)Na(2)	10	HexNAc(4)Hex(5)Fuc(1)NeuAc(1)Na(1)
N331	3	HexNAc(3)Hex(6)Fuc(1)NeuAc(1)	3	HexNAc(3)Hex(4)NeuAc(1)	2	HexNAc(4)Hex(5)Fuc(1)NeuAc(1)Na(1)	0	N/A
N343	4	HexNAc(4)Hex(5)NeuAc(2)Na(1)	6	HexNAc(4)Hex(5)NeuAc(2)Na(1)	4	HexNAc(4)Hex(5)NeuAc(2)Na(1)	7	HexNAc(6)Hex(3)Fuc(1)NeuAc(2)
N603	12	HexNAc(4)Hex(5)Fuc(1)NeuAc(1)Na(1)	7	HexNAc(4)Hex(5)Fuc(1)NeuAc(2)Na(1)	16	HexNAc(6)Hex(3)Fuc(1)NeuAc(1)	3	HexNAc(5)Hex(5)NeuAc(1)
N616	13	HexNAc(4)Hex(5)Fuc(1)NeuAc(2)	9	HexNAc(4)Hex(5)NeuAc(1)Na(1)	18	HexNAc(4)Hex(5)Fuc(1)NeuAc(2)	2	HexNAc(2)Hex(9)
N657	0	N/A	0	N/A	5	HexNAc(6)Hex(3)Fuc(1)NeuAc(2)	0	N/A
N709	5	HexNAc(4)Hex(6)Fuc(1)NeuAc(1)Na(1)	1	HexNAc(5)Hex(6)NeuAc(1)	17	HexNAc(4)Hex(5)Fuc(1)NeuAc(2)	3	HexNAc(4)Hex(5)NeuAc(1)
N717	14	HexNAc(4)Hex(5)Fuc(1)NeuAc(2)	7	HexNAc(4)Hex(5)Fuc(1)NeuAc(1)Na(1)	25	HexNAc(6)Hex(3)Fuc(1)NeuAc(2)	4	HexNAc(4)Hex(5)Fuc(1)NeuAc(2)Na(2)
N801	44	HexNAc(4)Hex(5)Fuc(1)NeuAc(1)	46	HexNAc(4)Hex(5)Fuc(1)NeuAc(1)	42	HexNAc(6)Hex(3)Fuc(1)NeuAc(1)	40	HexNAc(3)Hex(6)Fuc(1)NeuAc(1)
N1074	0	N/A	7	HexNAc(4)Hex(5)NeuAc(2)Na(1)	1	HexNAc(4)Hex(5)NeuAc(1)	7	HexNAc(4)Hex(5)Fuc(1)NeuAc(1)
N1098	50	HexNAc(4)Hex(5)Fuc(1)NeuAc(2)Na(2)	52	HexNAc(4)Hex(5)Fuc(1)NeuAc(1)	52	HexNAc(4)Hex(5)Fuc(1)NeuAc(2)Na(2)	49	HexNAc(4)Hex(5)Fuc(1)NeuAc(2)
N1134	5	HexNAc(4)Hex(5)NeuAc(2)Na(1)	12	HexNAc(4)Hex(6)Fuc(1)NeuAc(1)	21	HexNAc(6)Hex(3)Fuc(1)NeuAc(1)	5	HexNAc(3)Hex(6)Fuc(1)NeuAc(1)
N1158	12	HexNAc(4)Hex(5)Fuc(1)NeuAc(1)	6	HexNAc(4)Hex(5)NeuAc(2)Na(1)	7	HexNAc(4)Hex(4)NeuAc(1)	9	HexNAc(4)Hex(5)Fuc(1)NeuAc(1)
N1173	11	HexNAc(6)Hex(3)Fuc(1)NeuAc(2)	6	HexNAc(6)Hex(4)NeuAc(1)	7	HexNAc(6)Hex(3)Fuc(1)NeuAc(2)	9	HexNAc(6)Hex(3)Fuc(1)NeuAc(2)
N1194	23	HexNAc(4)Hex(5)NeuAc(2)Na(2)	30	HexNAc(4)Hex(5)Fuc(1)NeuAc(1)	27	HexNAc(4)Hex(5)Fuc(1)NeuAc(1)	14	HexNAc(4)Hex(5)Fuc(1)NeuAc(1)

Glycosylation profile of SARS-CoV-2 spike variants. N-linked glycans were identified by mass spectrometry. The number of glycans identified at each site and an example glycan are reported.

Table S2.

A

Number of spectral peaks in bimodal peptides at deuterium exchange time = 1 min					
Peptide	**WT**	**D614G**	**Alpha**	**Delta**	**Omicron (BA.1)**
553-568	15	13	13	13	13
875-882	7.5 ± 0.5	6	6.3 ± 0.57	5.6 ± 0.57	3.3 ± 0.57
900-913	12	10	10	9.6 ± 0.57	10
943-958	14.5 ± 0.5	13.3 ± 1.15	13	13.6 ± 0.57	-
988-998	9	6.3 ± 0.57	5	6.6 ± 0.57	6.3 ± 0.57

B

Number of spectral peaks in bimodal peptides at deuterium exchange time = 10 min					
Peptide	**WT**	**D614G**	**Alpha**	**Delta**	**Omicron (BA.1)**
553-568	14	13	13	13	14
875-882	8	6.3 ± 0.57	7	6.3 ± 0.57	3
900-913	15	13	13	11	12
943-958	16	15.6 ± 0.57	16	12	-
988-998	10.3 ± 0.57	7.6 ± 1.15	5.3 ± 0.57	8±1	8

Differential ensemble behavior across S variants inferred from spectral broadening. A) Table showing spectral broadening at Dex = 1 min B) Table showing spectral broadening at Dex = 10 min. The number of spectral peaks were determined based on the assigned sticks during HDXMS analysis across common peptides.

Table S3.

Peptide	Sequence	D614G – WT (ΔDex)	Alpha – WT (ΔDex)	Delta – WT (ΔDex)	Omicron – WT (ΔDex)
177-191	MDLEGKQGNFKNLRE	0.5 ± 0.2 Da	1.1 ± 0.2 Da	-0.2 ± 0.2 Da	0.3 ± 0.2 Da
245-265	HRSYLTPGDSSSGWTAGAAAY	0.7 ± 0.4 Da	0.6 ± 0.4 Da	-0.6 ± 0.5 Da	1.1 ± 0.3 Da
456-467	FRKSNLKPFERD	0.2 ± 0.1 Da	0.0 ± 0.1 Da	0.0 ± 0.1 Da	0.5 ± 0.1 Da

Differences in NTD deuterium uptake comparing D614G and variants with WT at Dex = 30 min.

Table S4.

Peptide	Sequence	Variant	Δ Da 1 min	Δ Da 2 min	Δ Da 10 min	Δ Da 30 min
92-103	FAS**I**EKSNIIRG	Omicron	-0.2 ± 0.1	0.2 ± 0.1	0.9 ± 0.1	0.9 ± 0.1
401-420	VIRGDEVRQIAPGQTG**N**IAD	Omicron	0.6 ± 0.3	0.7 ± 0.3	0.5 ± 0.3	0.3 ± 0.3
401-421	VIRGDEVRQIAPGQTG**N**IADY	Omicron	0.5 ± 0.3	0.9 ± 0.3	0.4 ± 0.3	0.3 ± 0.3
407-420	VRQIAPGQTG**N**IAD	Omicron	0.6 ± 0.2	0.7 ± 0.2	0.5 ± 0.2	0.5 ± 0.2
407-421	VRQIAPGQTG**N**IADY	Omicron	0.5 ± 0.3	0.8 ± 0.3	0.6 ± 0.3	0.3 ± 0.3
407-422	VRQIAPGQTG**N**IADYN	Omicron	-0.4 ± 0.1	-0.3 ± 0.1	-0.1 ± 0.1	0.1 ± 0.1
442-452	DSKV**S**GNYNYL	Omicron	0.3 ± 0.2	0.5 ± 0.2	0.1 ± 0.2	-0.2 ± 0.2
444-452	KV**S**GNYNYL	Omicron	-1.5 ± 0.2	-1.3 ± 0.2	-1.2 ± 0.2	-1.1 ± 0.2
542-552	NFNGL**K**GTGVL	Omicron	-0.2 ± 0.1	-0.2 ± 0.1	-0.5 ± 0.1	-0.5 ± 0.1
544-552	NGL**K**GTGVL	Omicron	0.1 ± 0.1	0.0 ± 0.1	-0.2 ± 0.1	-0.2 ± 0.1
569-582	I**D**DTTDAVRDPQTL	Alpha	-0.2 ± 0.3	-0.3 ± 0.3	-0.4 ± 0.3	-0.5 ± 0.3
761-768	**K**RALTGIA	Omicron	-0.2 ± 0.2	-0.1 ± 0.2	-0.2 ± 0.2	-0.3 ± 0.2
780-793	AQVKQIYKTPPIK**Y**	Omicron	-0.2 ± 0.3	-0.1 ± 0.3	-0.1 ± 0.3	-0.2 ± 0.3
943-958	GKLQ**N**VVNQNAQALNT	Delta	1.1 ± 0.4	0.3 ± 0.4	0.2 ± 0.4	-0.2 ± 0.4
943-958	GKLQ**N**VVNQNAQALNT	Omicron	-1.9 ± 0.3	-1.3 ± 0.3	-1.3 ± 0.3	-1.7 ± 0.3
959-967	LVKQLSS**K**F	Omicron	0.8 ± 0.1	0.8 ± 0.1	0.2 ± 0.1	0.1 ± 0.1
959-974	LVKQLSS**K**FGAISSVL	Omicron	2.1 ± 0.3	1.9 ± 0.3	1.9 ± 0.3	1.7 ± 0.3
977-987	IL**A**RLDPPEAE	Alpha	-0.8 ± 0.2	-0.7 ± 0.2	-0.4 ± 0.2	-0.1 ± 0.2
977-987	I**F**SRLDPPEAE	Omicron	0.7 ± 0.2	0.5 ± 0.2	-0.2 ± 0.2	-0.4 ± 0.2
979-987	**A**RLDPPEAE	Alpha	-0.4 ± 0.2	-0.4 ± 0.2	-0.9 ± 0.2	-1.0 ± 0.2
979-989	**A**RLDPPEAEVQ	Alpha	-0.6 ± 0.2	-0.4 ± 0.2	-0.5 ± 0.2	-0.4 ± 0.2

HDXMS analysis of mutated peptides. Differences between variants and D614G S for mutated peptides reported in Da for 1, 2, 10, and 30 min exchange. Mutations sites are shown in bold red. Type or paste caption here.

A

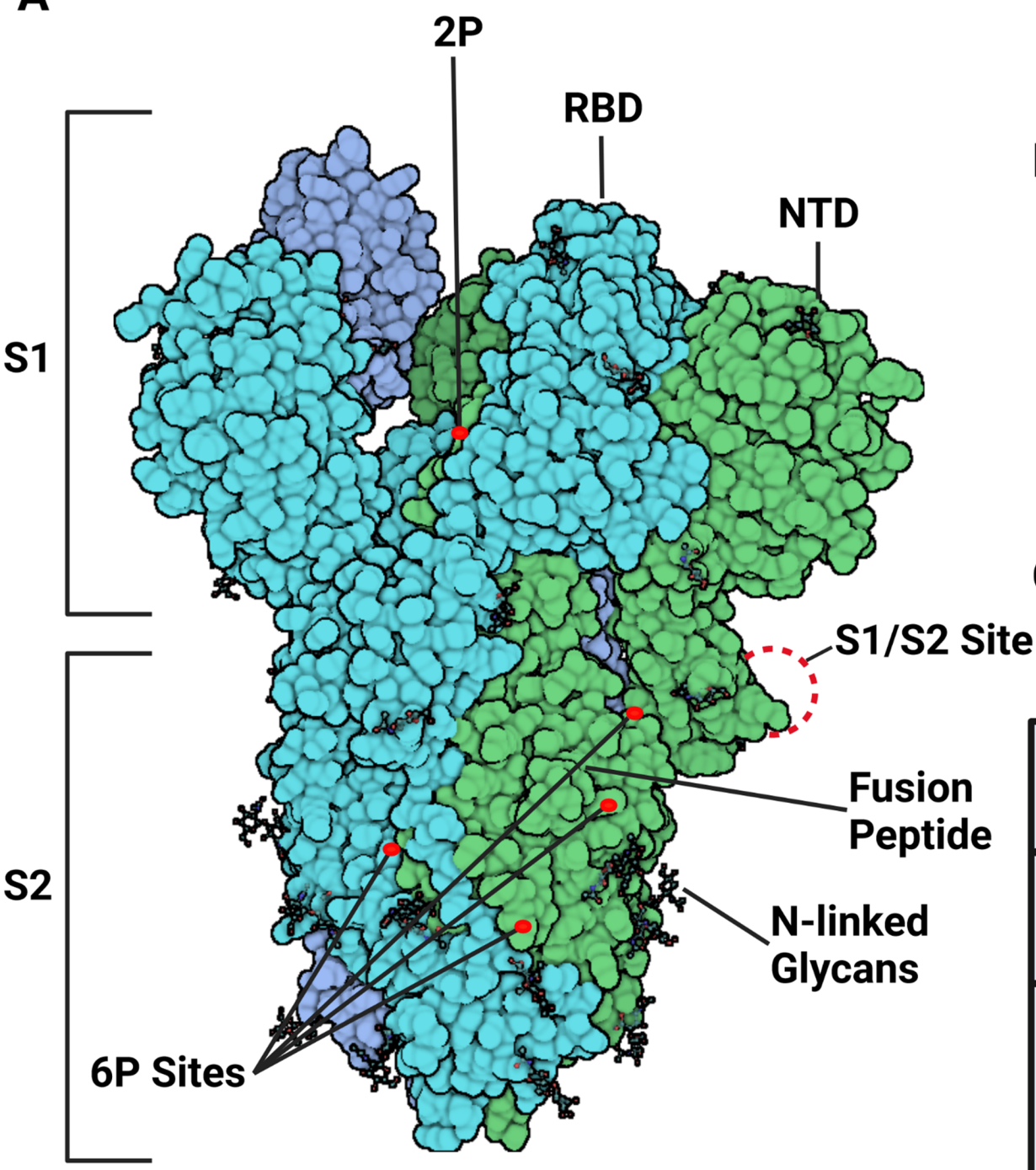

B

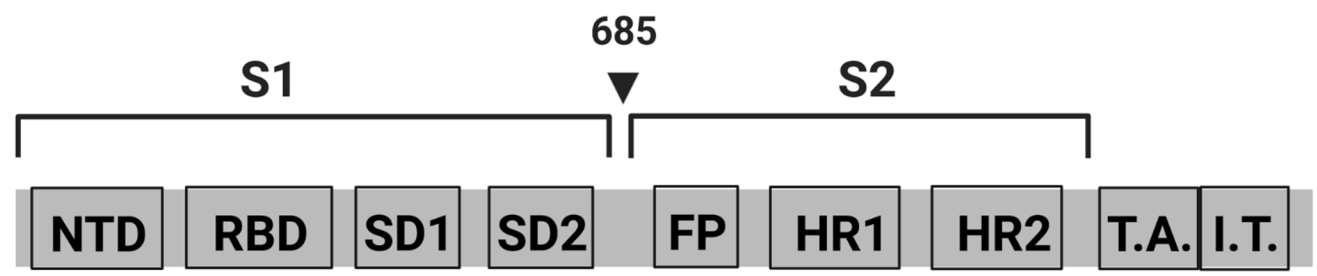

C

	NTD	RBD	S1	S2
Alpha	Δ69-70, Δ144	N501Y	A570D, **D614G**, P681H	T716L, S982A, D1118A
Delta	T19R, Δ157-158	L452R, T478K	**D614G**, P681R	D950N
Omicron (BA.1)	A67V, Δ69-70, T95I, ins214EPE, Δ211, L212I	G339D, S371L, S373P, S375F, K417N, N440K, G446S, S477N, T4978K, N501Y, Y505H	T547K, **D614G**, H655Y, N679K, P681H	N764K, D796Y, N856K, Q954H, N969K, L981F

A

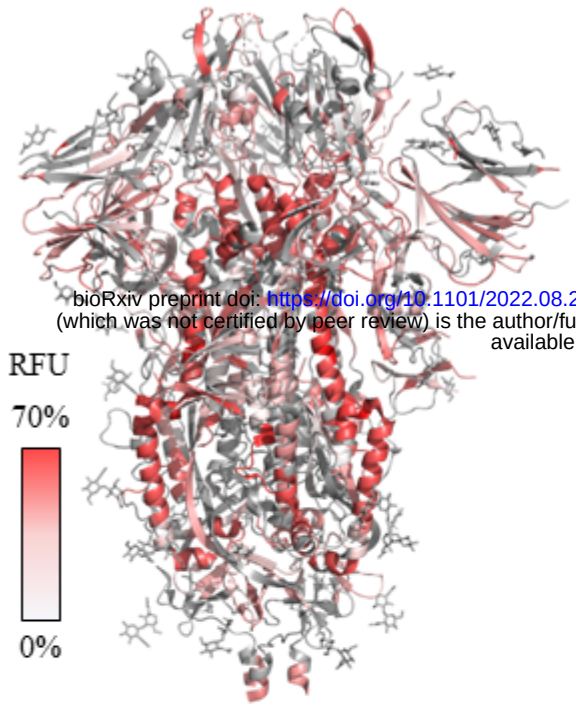

B

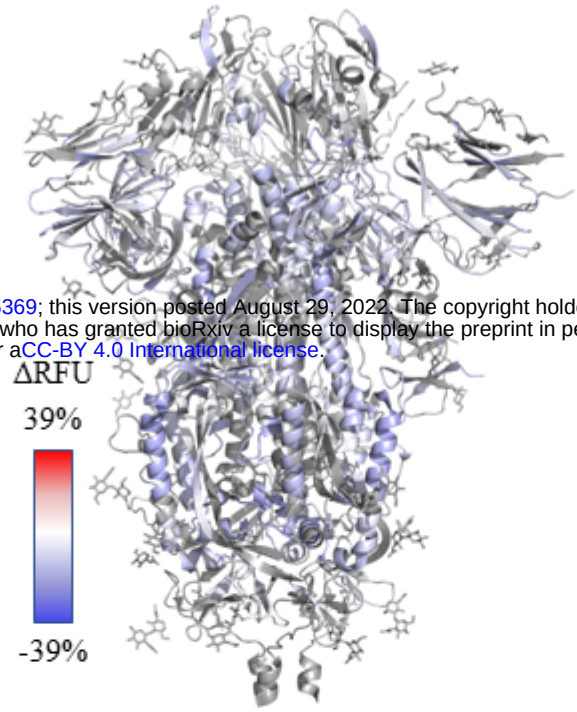

C

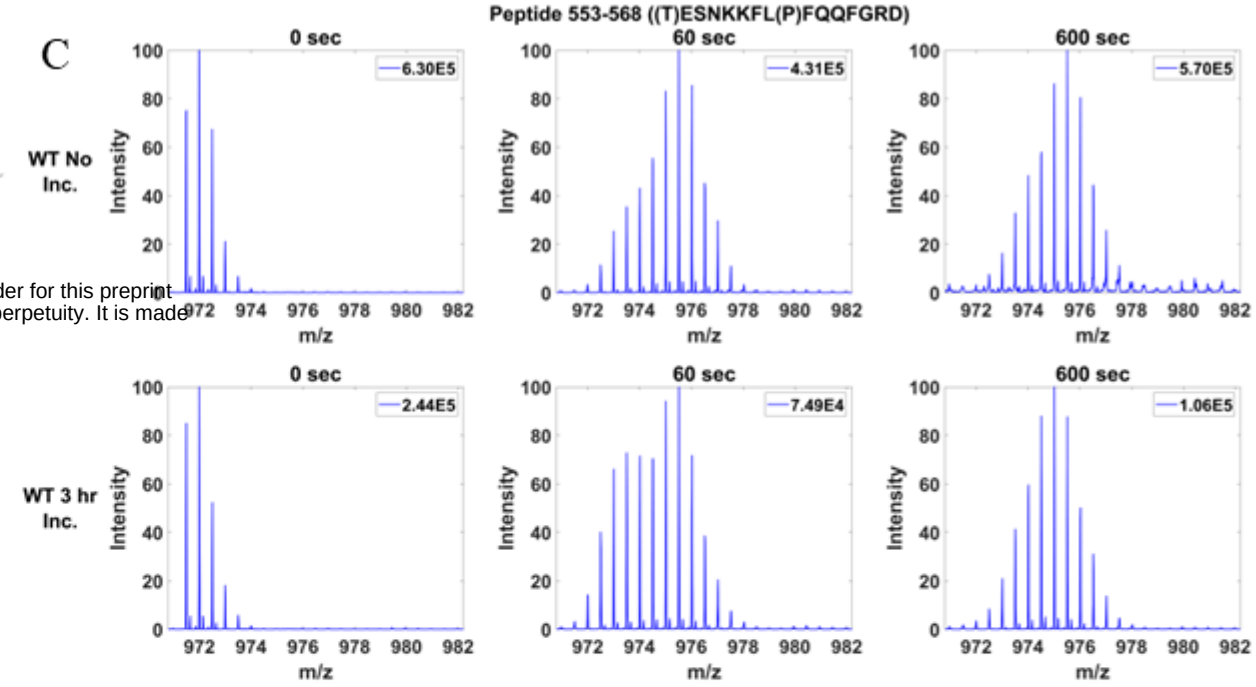

D

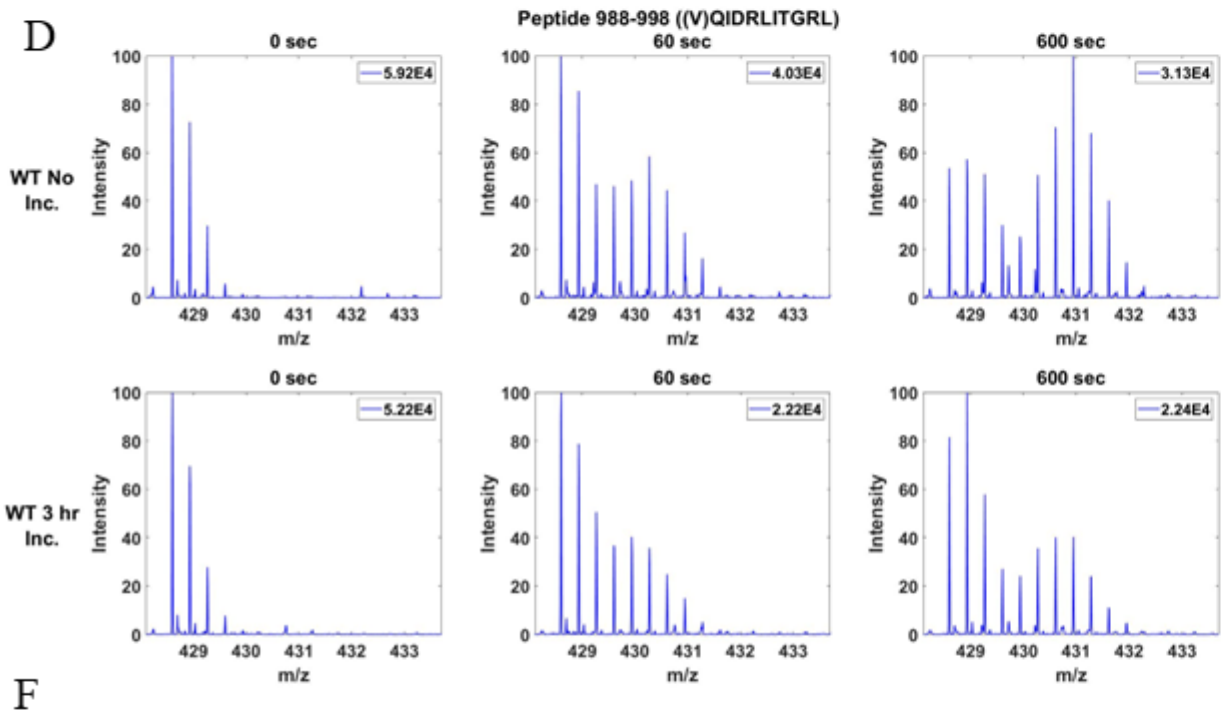

E

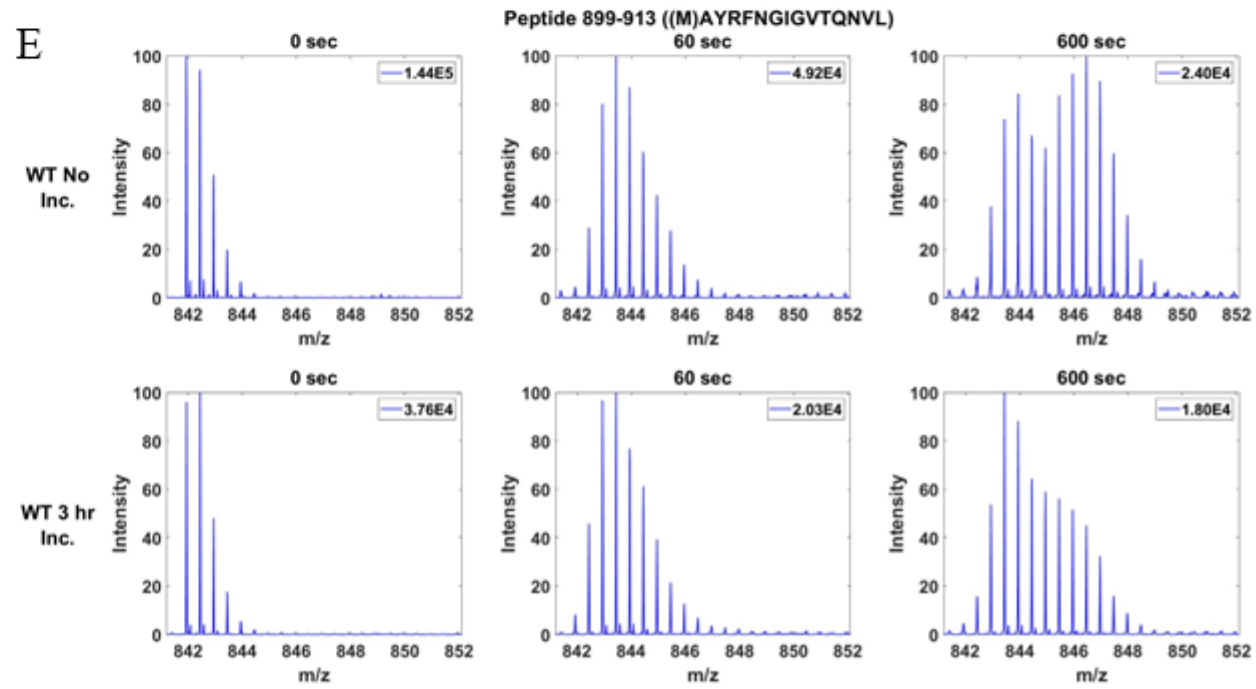

F

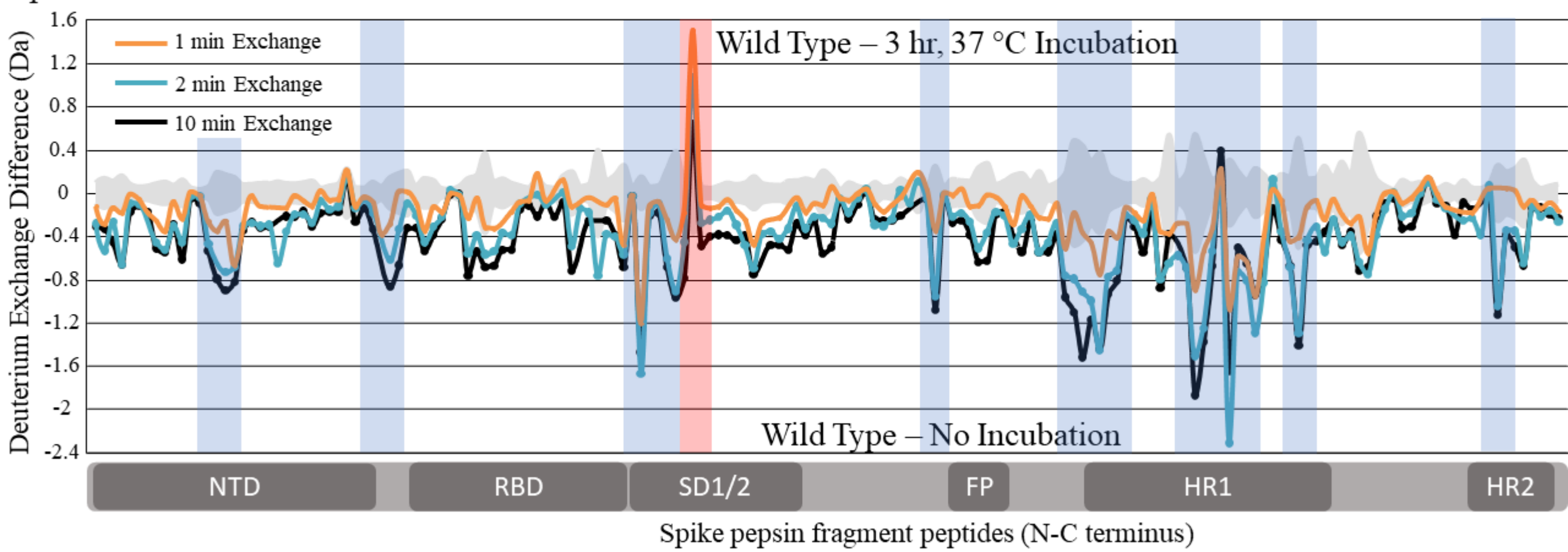

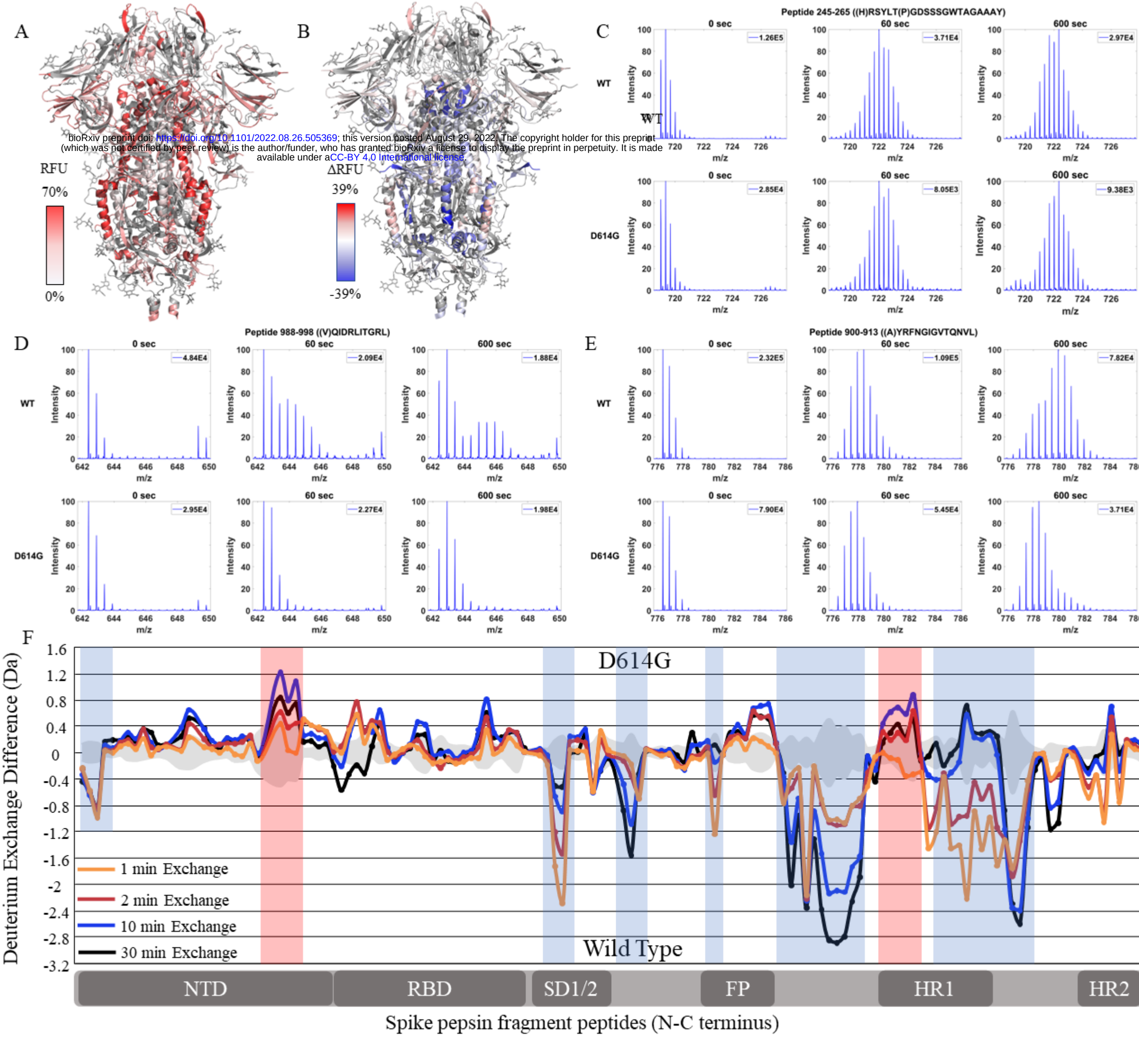

A

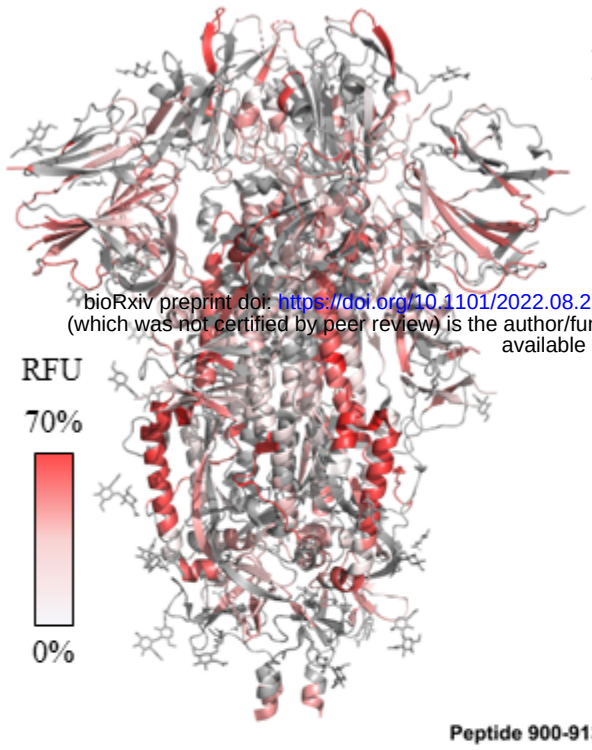

B

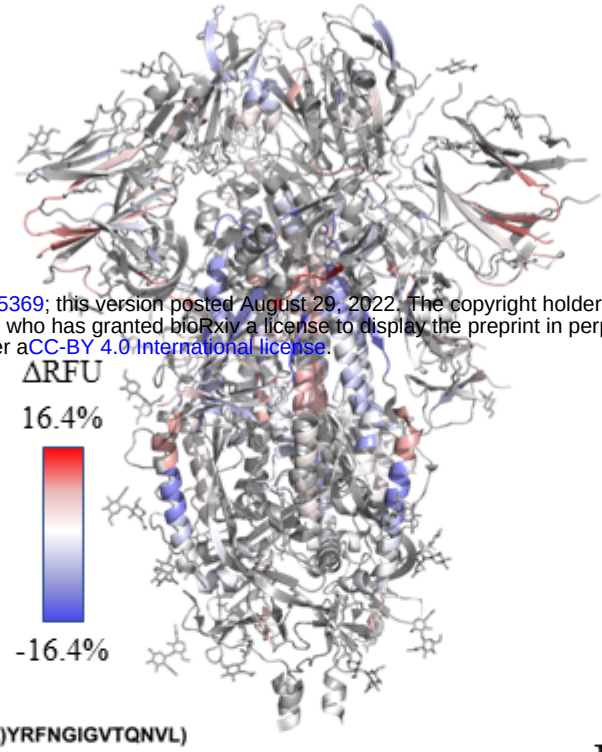

C

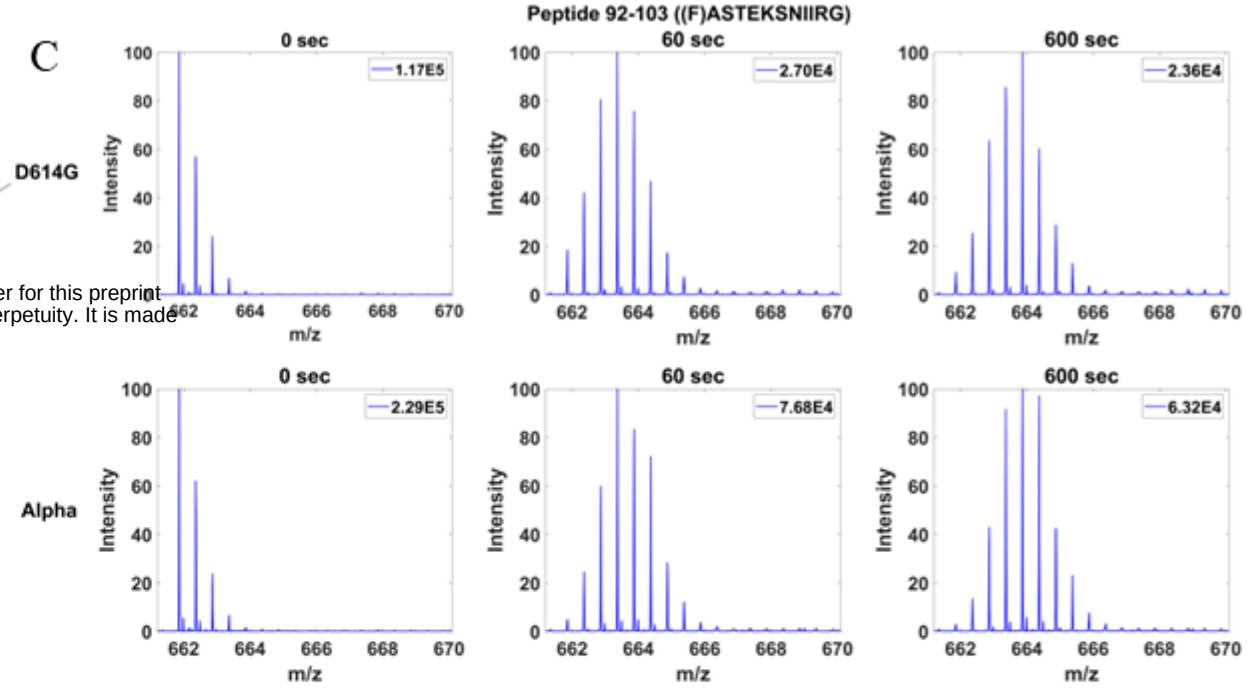

D

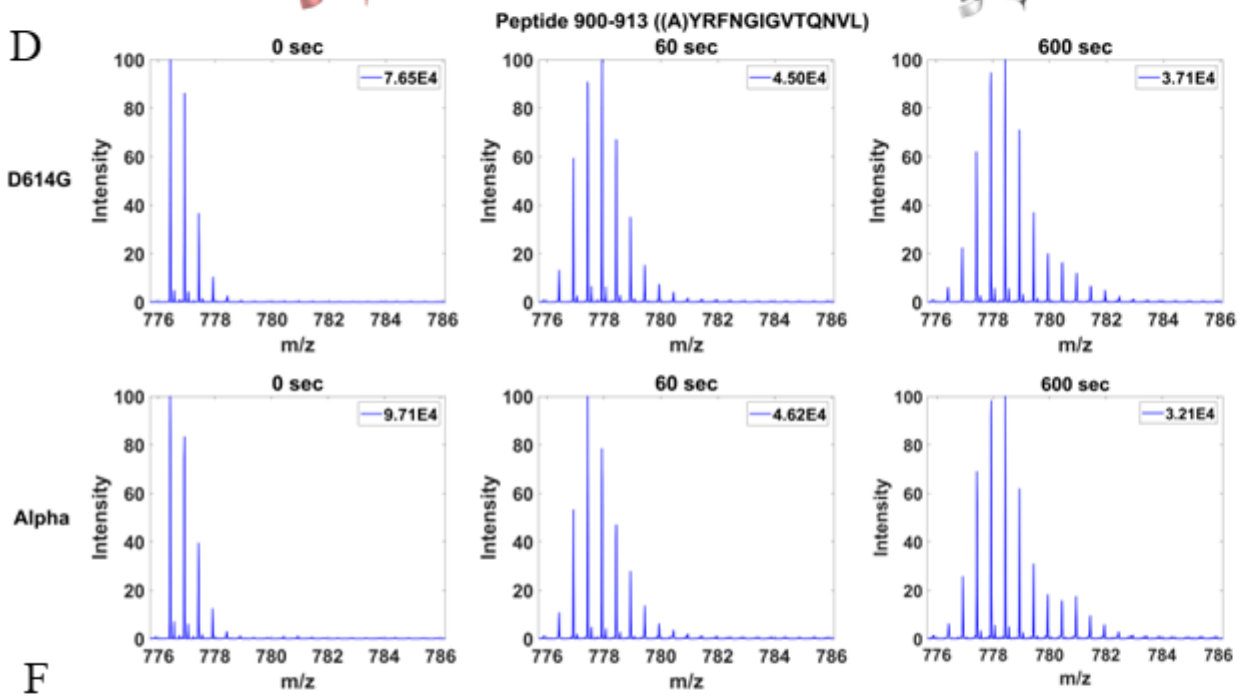

E

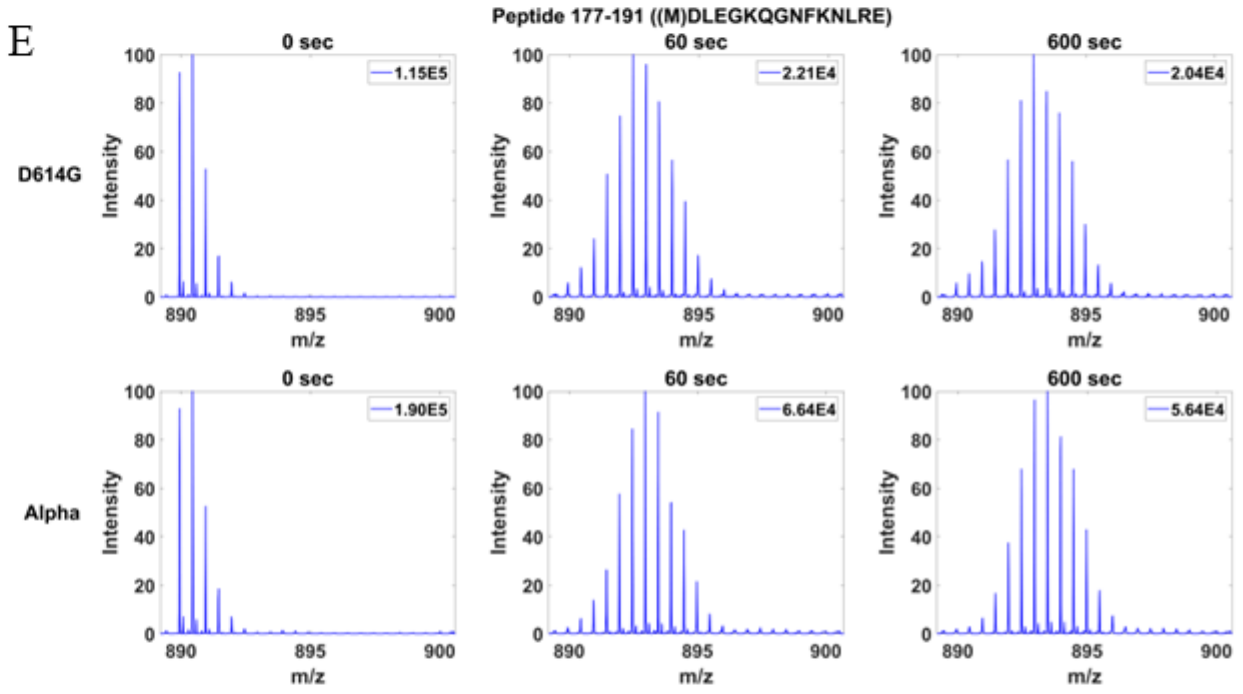

F

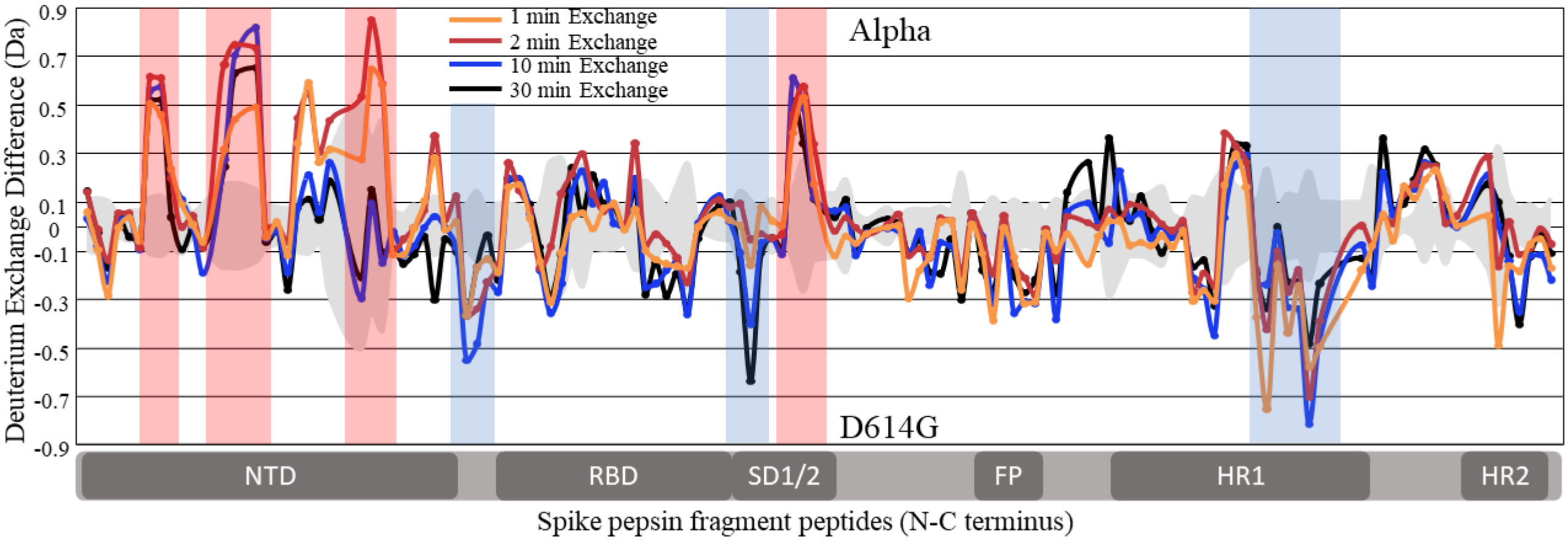

A

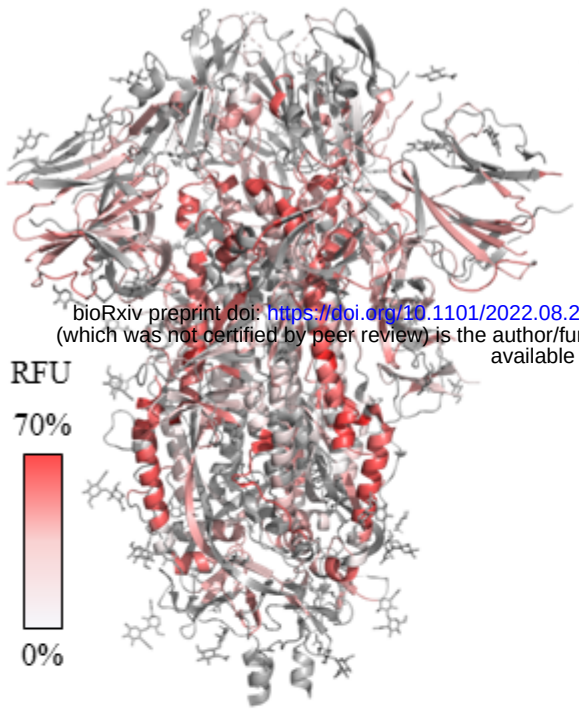

B

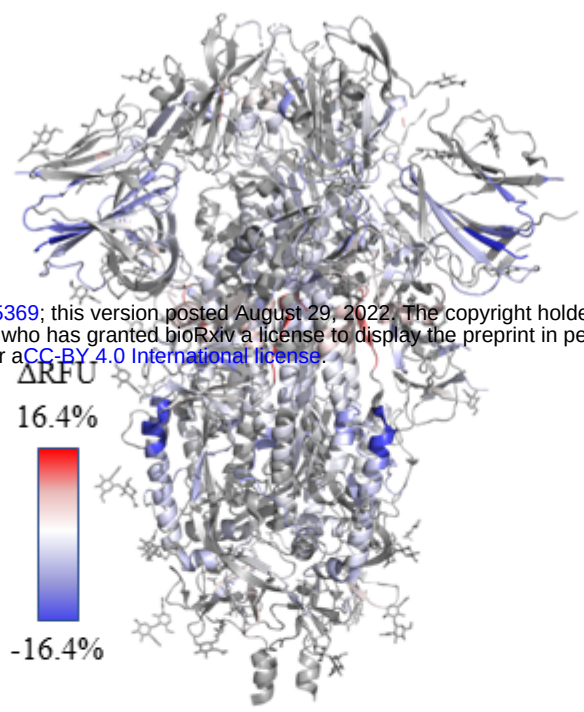

C

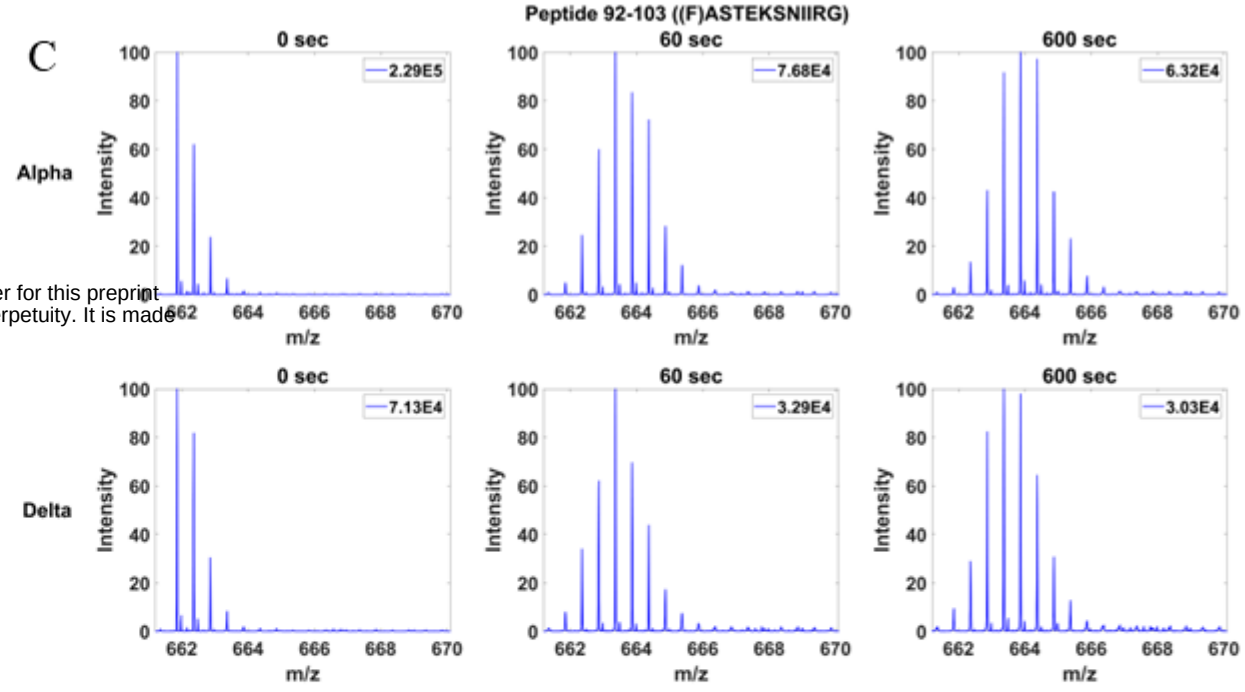

D

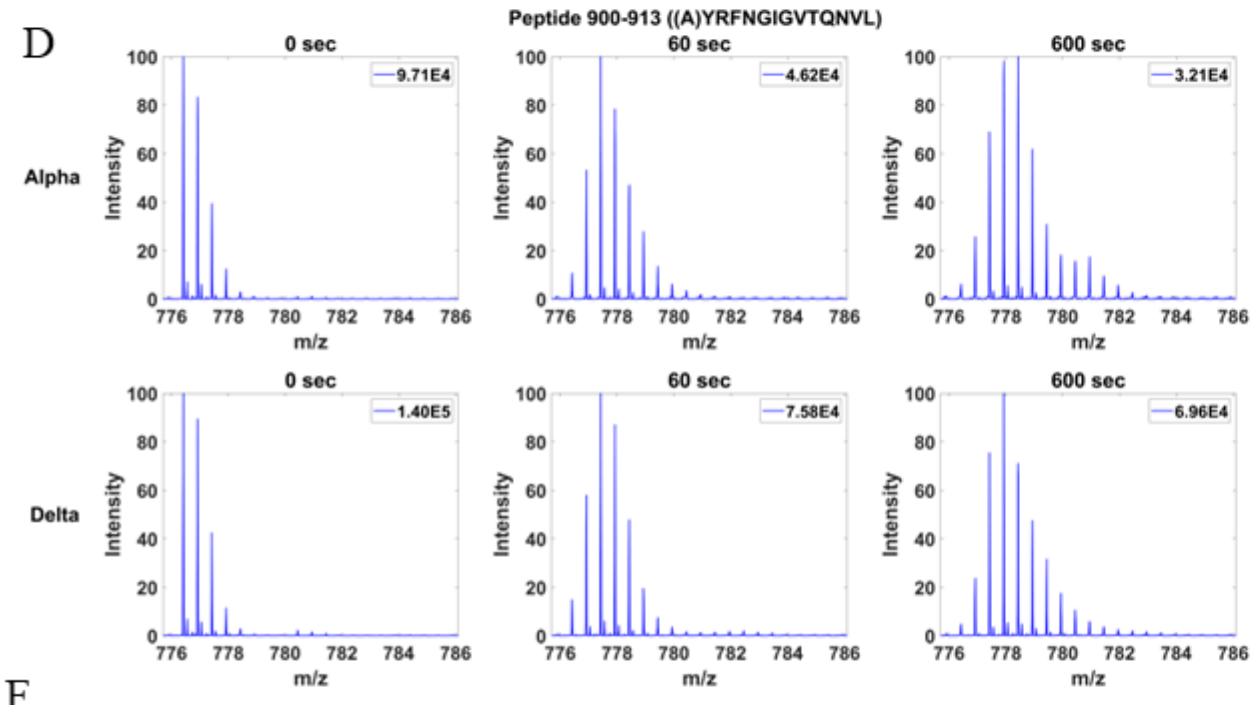

E

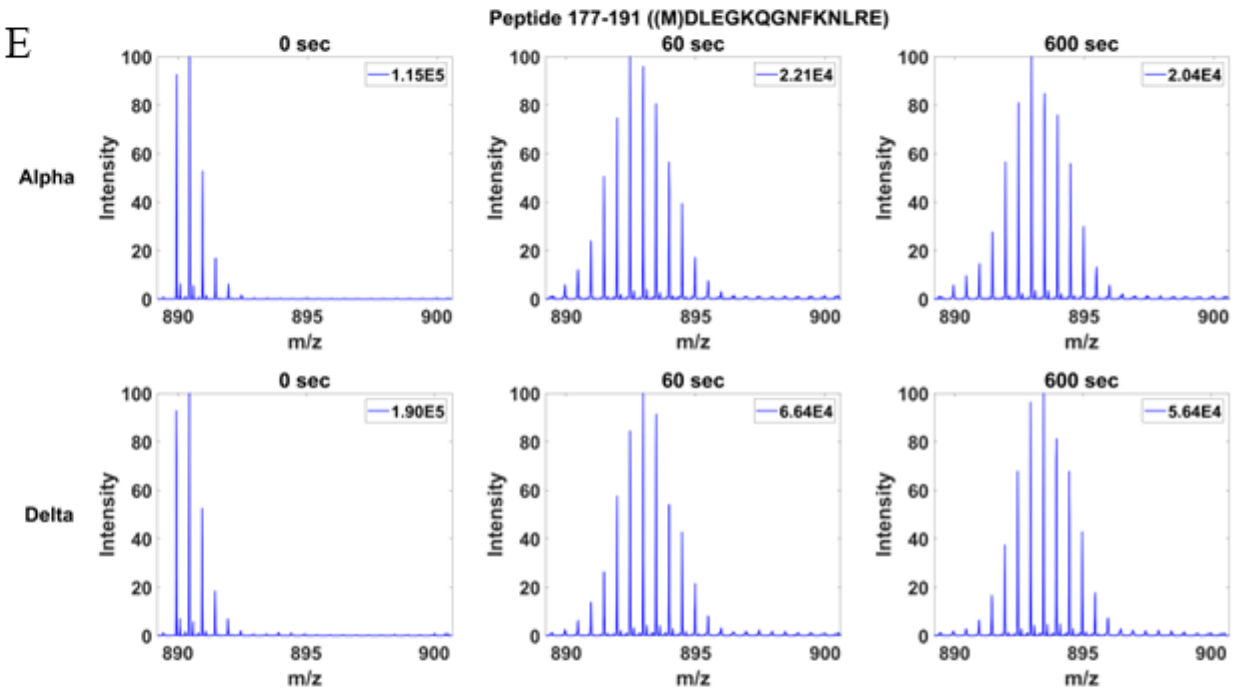

F

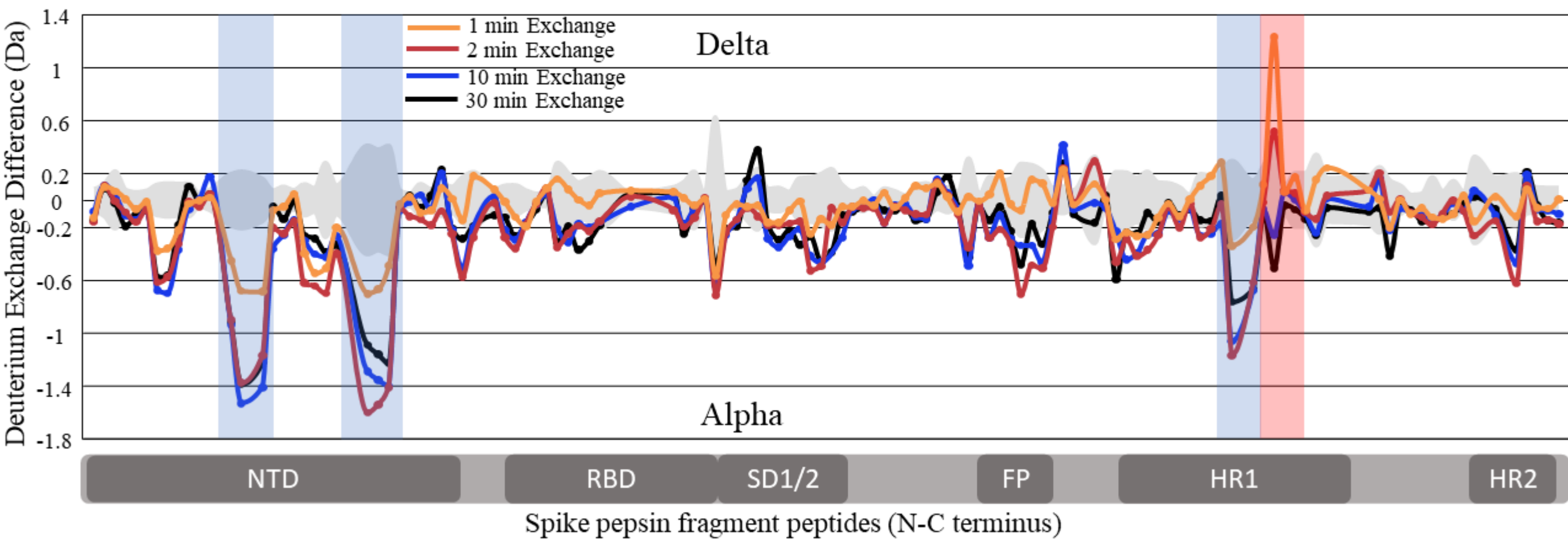

A

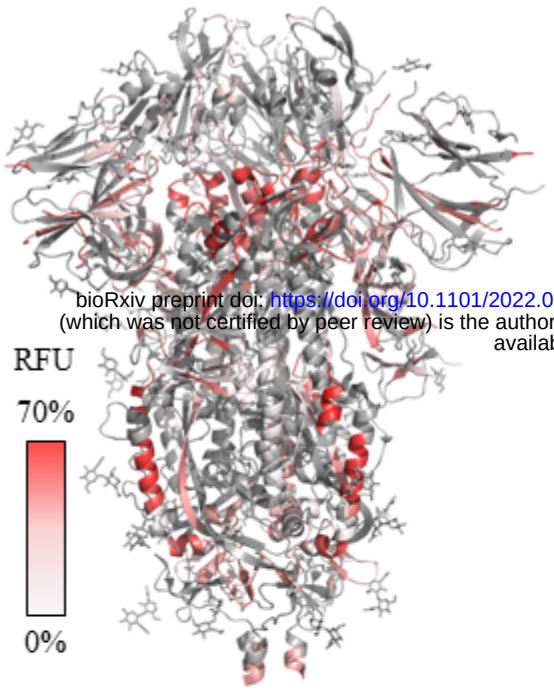

B

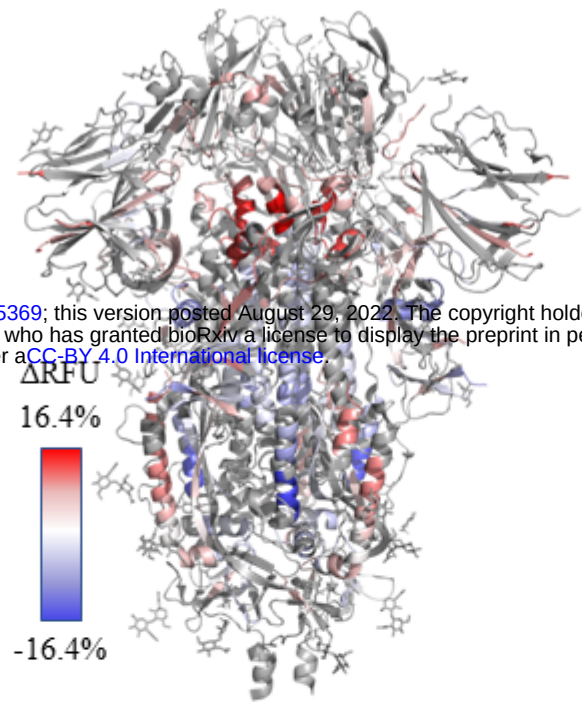

C

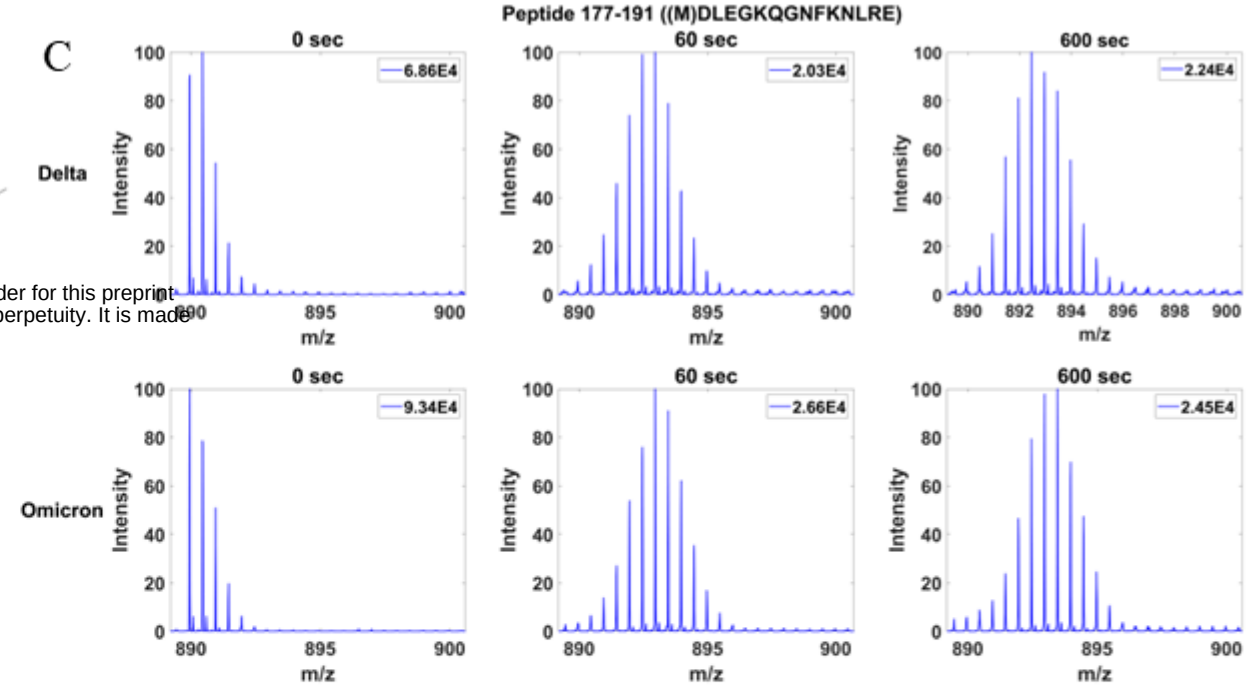

D

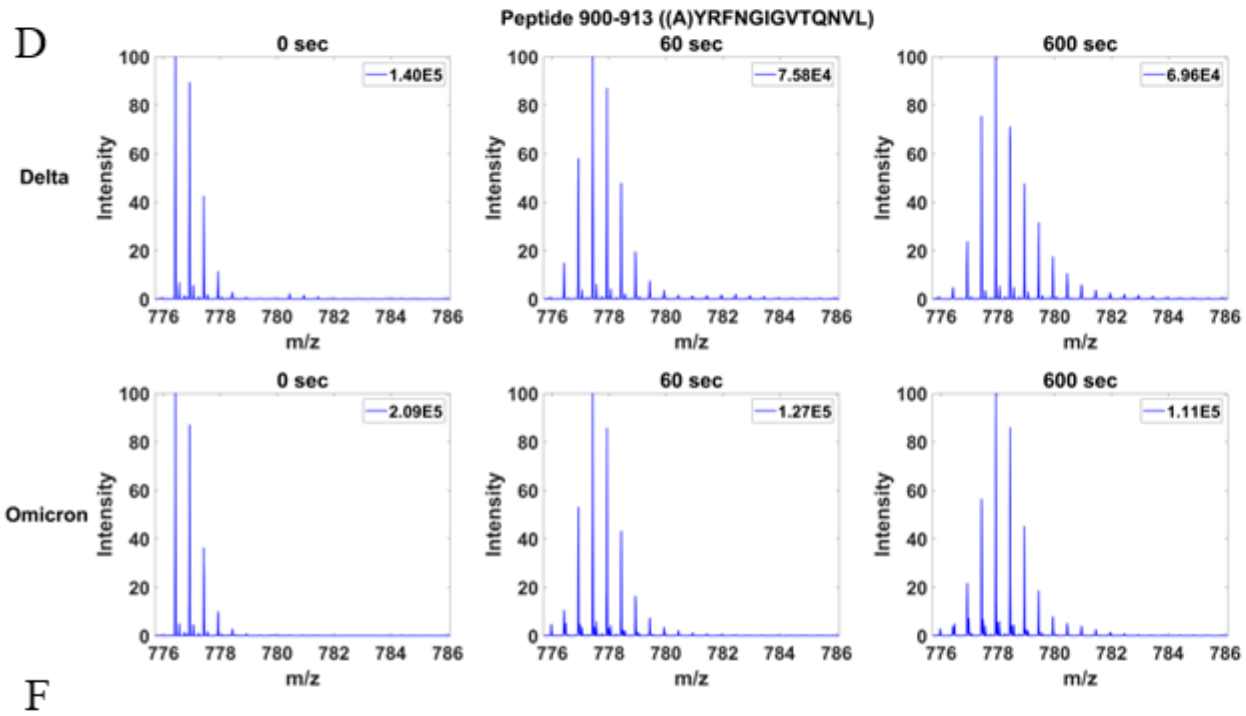

E

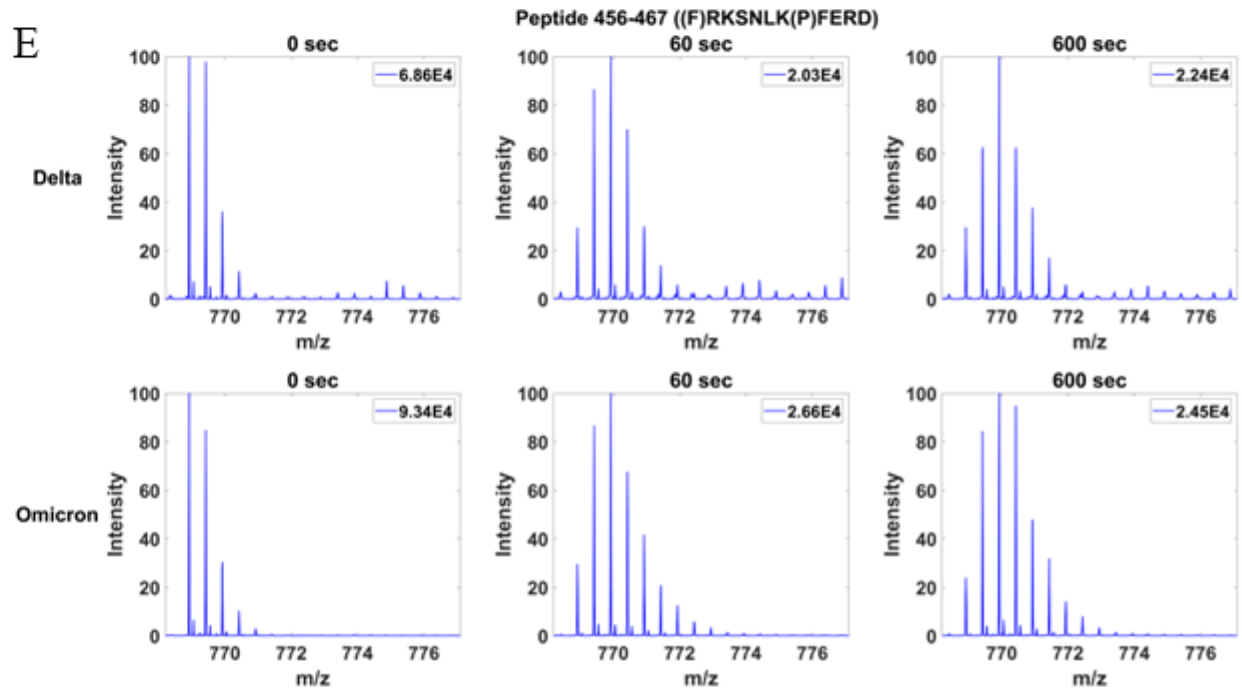

F

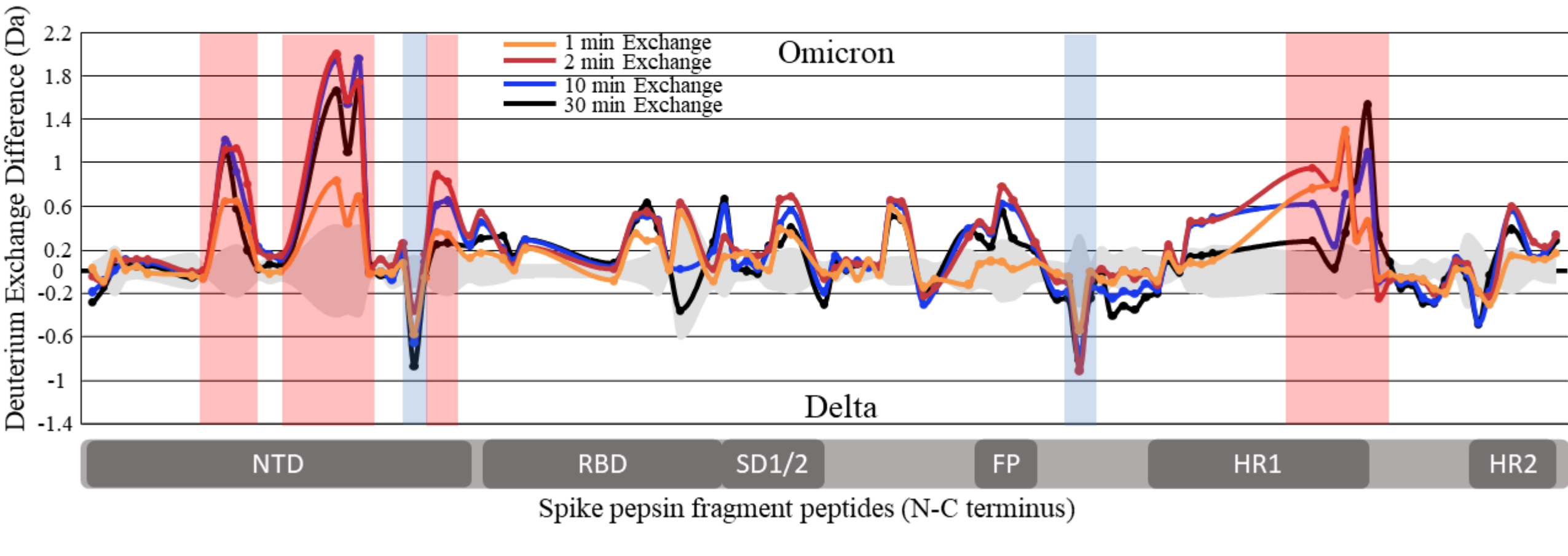

A

One RBD up

Two RBD down

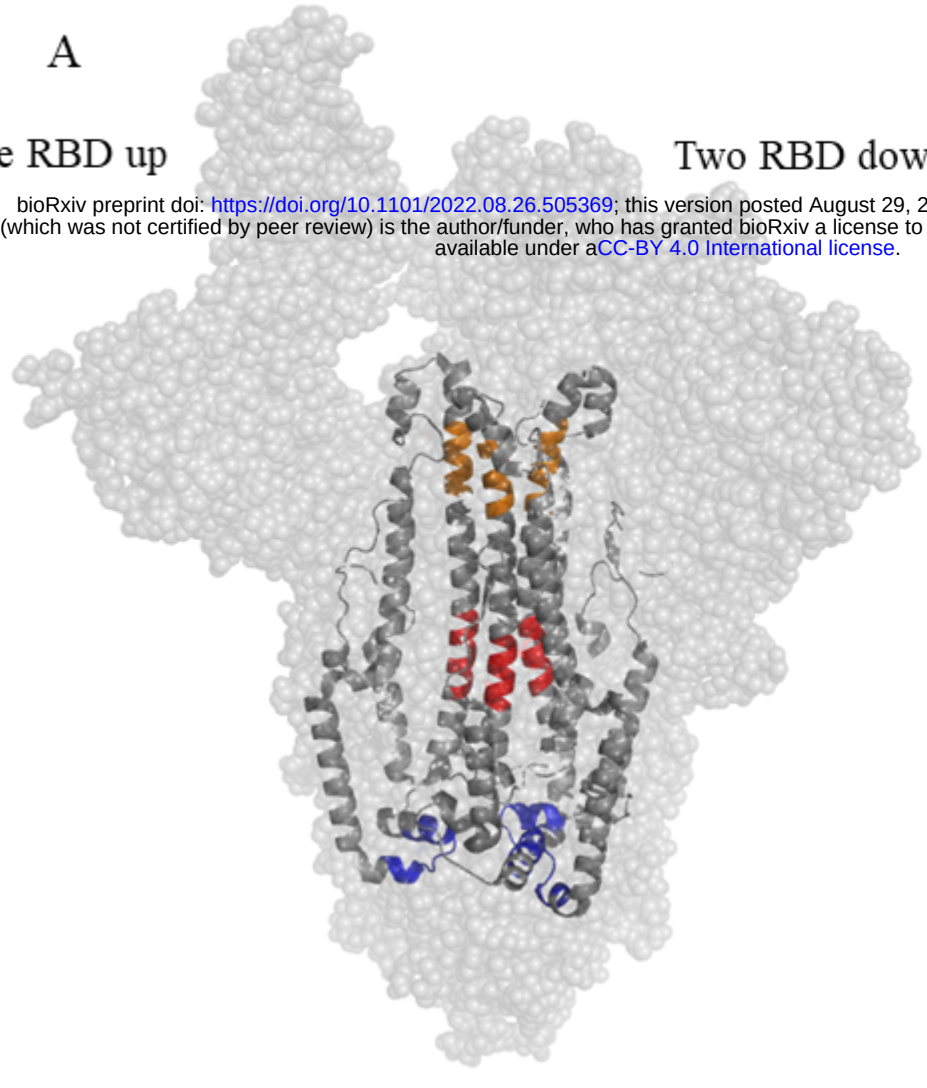

B

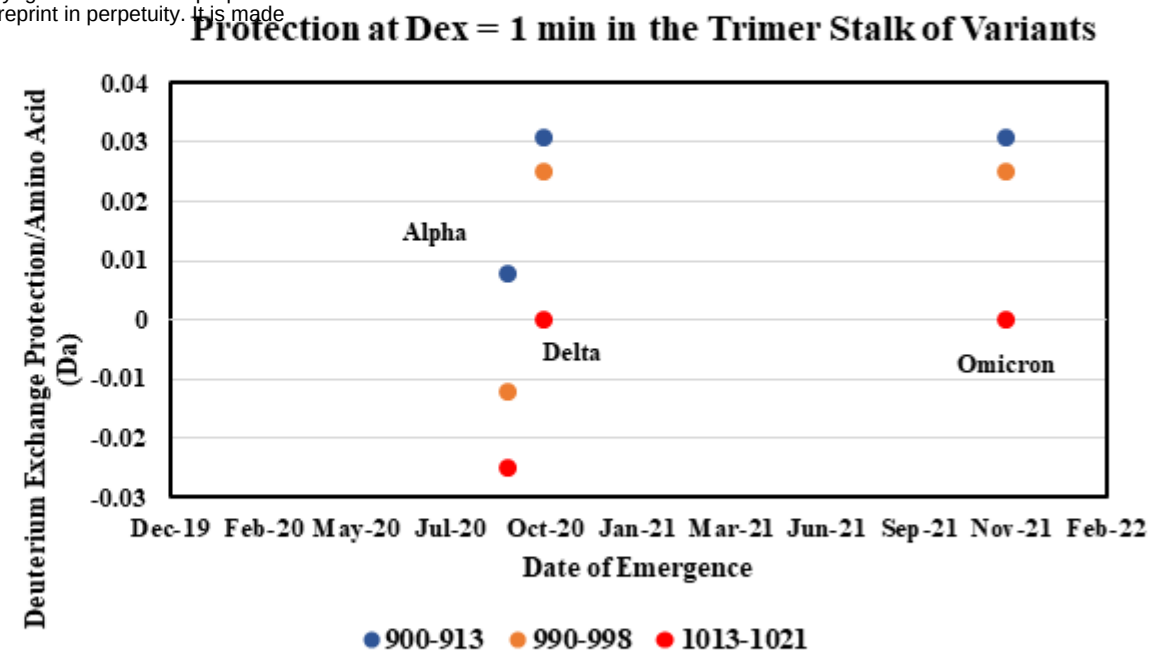

C

One RBD up

Two RBD down

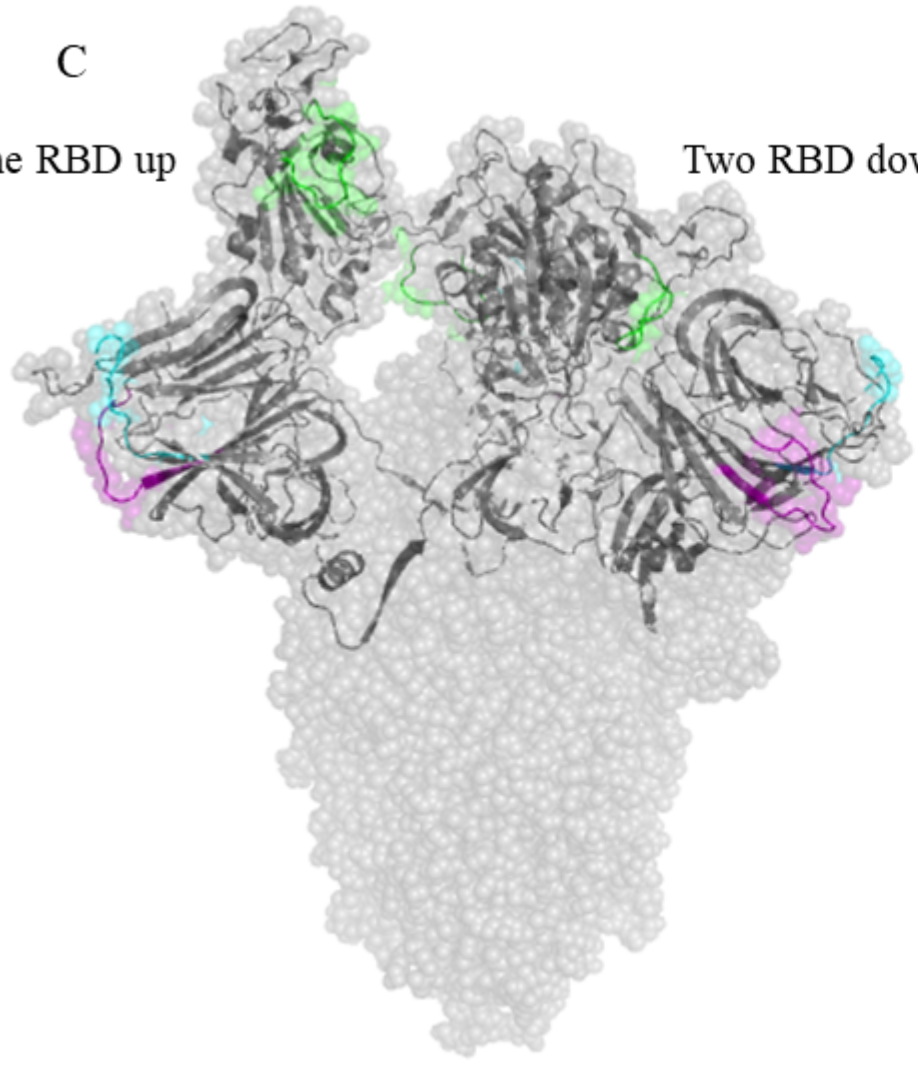

D